The Journal of Undergraduate Research in Physics

Volume 14, Number 2
May, 1996

Published by the Physics Department of Guilford College
for
The American Institute of Physics and the Society of Physics Students

THE JOURNAL OF UNDERGRADUATE RESEARCH IN PHYSICS

This journal is devoted to research work done by undergraduate students in physics and its related fields. It is to be a vehicle for the exchange of ideas and information by undergraduate students. Information for students wishing to submit manuscripts for possible inclusion in the Journal follows.

ELIGIBILITY
The author(s) must have performed all work reported in the paper as an undergraduate student(s). The subject matter of the paper is open to any area of pure or applied physics or physics related field.

SPONSORSHIP
Each paper must be sponsored by a full-time faculty member of the department in which the research was done. A letter from the sponsor, certifying that the work was done by the author as an undergraduate and that the sponsor is willing to be acknowledged at the end of the paper, must accompany the manuscript if it is to be considered for publication.

SUBMISSION
Two copies of the manuscript, the letter from the sponsor and a telephone number or E-Mail address where the author can be reached should be sent to:

Dr. Rexford E. Adelberger, Editor
THE JOURNAL OF UNDERGRADUATE
RESEARCH IN PHYSICS
Physics Department
Guilford College
Greensboro, NC 27410

FORM
The manuscript should be typed, double spaced, on 8 1/2 x 11 inch sheets. Margins of about 1.5 inches should be left on the top, sides, and bottom of each page. Papers should be limited to fifteen pages of text in addition to an abstract (not to exceed 250 words) and appropriate drawings, pictures, and tables.

Manuscripts may be submitted on a disk that can be read by a MacIntosh™. The files must be compatible with MacWrite™, MicroSoft Word™ , PageMaker™ or WordPerfect™.

ILLUSTRATIONS
Line drawings should be made with black ink on plain white paper. Each figure or table must be on a separate sheet. Photographs must have a high gloss finish. If the submission is on a disk, the illustrations should be in PICT, TIFF or EPS format.

CAPTIONS
A brief caption should be provided for each illustration or table, but it should not be part of the figure. The captions should be listed together at the end of the manuscript

EQUATIONS
Equations should appear on separate lines, and may be written in black ink. We use EXPRESSIONIST™ to format equations in the Journal.

FOOTNOTES
Footnotes should be typed, double spaced and grouped together in sequence at the end of the manuscript.

PREPARING A MANUSCRIPT
A more detailed set of instructions for authors wishing to prepare manuscripts for publication in the Journal of Undergraduate Research in Physics can be found in the back of issue # 2 of each Volume.

SUBSCRIPTION INFORMATION

The Journal is published twice each academic year, issue # 1 appearing in November and issue # 2 in May of the next year. There are two issues per volume.

TYPE OF SUBSCRIBER	PRICE PER VOLUME
Individual	$US 5.00
Institution	$US 10.00

Foreign subscribers add $US 2.00 for surface postage, $US 10.00 for air freight.

Back issues may be purchased by sending $US 15.00 per volume to the editorial office.

To receive a subscription, send your name, address, and check made out to **The Journal of Undergraduate Research in Physics (JURP)** to the editorial office:

JURP
Physics Department
Guilford College
Greensboro, NC 27410

The Journal of Undergraduate Research in Physics is sent to each member of the Society of Physics Students as part of their annual dues.

THE EFFECTS OF DISTRIBUTIONS OF SCATTERERS ON COMPRESSIONAL ULTRASONIC WAVES

Eric J. Carr *
Department of Physics
Stetson University
DeLand, FL 32720
received July 30, 1994

ABSTRACT

We measured the effects of various scattering distributions on compressional waves. Ultrasonic longitudinal pulses were propagated through three dimensional acrylic models. Holes drilled in the models acted as scattering centers. Both isotropic and anisotropic scattering patterns were produced. The scattering centers could be filled with water, air or other fillers. We measured the intensity of the ultrasound at various angles relative to the orientation of the scatterer distribution. The scattering was analyzed by comparing the spectral ratios generated by fast Fourier transforms of the data. We found, in the case of the water-filled scattering centers, evidence of constructive and destructive interference caused by the differences in the velocity of sound waves in acrylic and water.

INTRODUCTION

Natural seismic phenomena such as earthquakes and volcanic eruptions, as well as synthesized seismic events such as dynamite explosions, allow for the mapping of the interior of the earth. These maps show the location and type of fractures within and between the different layers of the earth. The behavior of the scattered seismic waves can even let us know if the fractures are filled with liquids or other solids. Physical models are often used to test theories of the propagation of seismic waves in the earth. [1] Scattering centers are placed within the model to represent fractures. Ultrasonic waves are used to model the behavior of seismic waves as they scatter from the faults in the model earth.

When scatterers are placed in a model, the propagating waves strike them, either passing through them or reflecting in all directions. The reduces the amount of energy that strikes the receiving transducer. In some instances, the reflected energy also finds its way to the receiver. In both cases, the waves arrive later than the initial pulse and have less intensity. This spread in time of the wave can be seen in what is called the coda, the energy that follows the initial pulse. For compressional waves, the coda contains information about the propagation of the waves through the liquids.

There are three principles that affect the loss of intensity of a compressional waves as it passes through a medium. Geometrical spreading results from the waves traveling in many directions, not just towards the receiver. This disperses the energy in the wave. Intrinsic attenuation is the medium's natural resistance to particle motion. In this case, energy is absorbed by the molecules of the medium. This energy is lost as heat. The third effect, apparent attenuation, energy is lost due to interactions with the scatterers in the medium. The loss is a function of the number, type and position of the scatterers within the sample. To analyze the effect of the fractures or scatterers on the wave, the first two must effects must be eliminated.

Another effect has to do with the plate properties of the material rather than bulk properties. Plate properties are observed in two-dimensional materials with height less than about one wavelength of the incident wave. For bulk materials, the height is usually an order of magnitude greater than the wavelength. Models with thicknesses between these designations exhibit a combination of characteristics. Compressional waves observed propagating through a material with these properties contain 'shadow pulses' which trail the initial pulse at regular

Eric received his B.Sc. in astrophysics from Stetson University in May of 1995. This research was completed during two summer research assistantships with Dr. Bruce Dubendorff at Stetson. Eric is currently working at Northwestern University and applying to their graduate program in the history and philosophy of science.

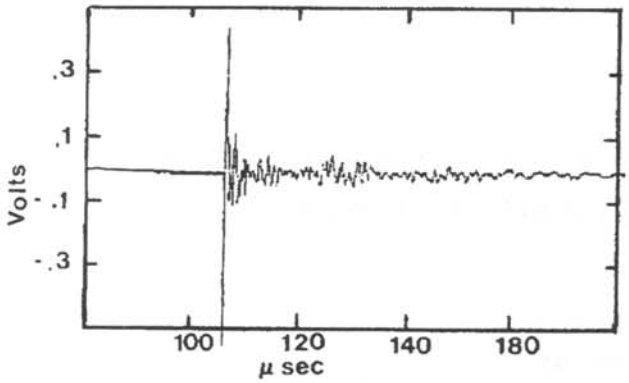

Figure 1

Voltage from the receiver as a function of time for a compressional wave with a significant coda. The data were collected from the circular model with 33 scatterers.

intervals. In plate materials, these 'shadow pulses' are indistinguishable from the initial pulse, but in bulk materials, these pulses should disappear completely.

THE EXPERIMENT

Models

The first step was to create a set of models to study. We produced three hexadecagonal acrylic models, each with a diameter of 200 mm. and a thickness of 51 mm. This allowed us to measure scattering at azimuthal angles from 0° to 180° in increments of 22.5° The scattering centers were produced by drilling holes in the acrylic material. The 51 mm thickness significantly reduced the plate properties of any scattering taking place.

The first model, the 'circular model', had an isotropic distribution of isotropic scatterers (3.2 mm diameter cylindrical holes). The second model, the 'aligned model', had an isotropic distribution of anisotropic scatterers (elliptical slots in the acrylic). The third model, the 'random model', contained an isotropic distribution of anisotropic scatterers. The isotropic and anisotropic scatterers were designed to have equal volume.

Apparatus

To minimize variations in the manner in which each waveform was generated and recorded, a table was built with mounts to hold the model and a track in which to place the ultrasonic transducers. The transducers were placed in nylon housings that fit into the tracks. Adjustable supports were placed at the ends of each track to ensure that the transducer could be set flush with the model and allow for the adjustment of the pressure used to hold the transducer in place.

Two transducers with center frequency of 2.25 MHz were used. A signal was sent to the source transducer by a pulser-receiver which was being triggered externally by a digital function generator set to 100 Hz. [2] The output of the receiver transducer was sent through the pulser-receiver to a digital oscilloscope.

Data Analysis

The two transducers were placed at opposite faces of each model. The pulser-receiver's attenuation settings were recorded. The amplitude of each waveform was then adjusted for this factor. Data were taken for each model before the scatterers were drilled into the models. Then data were taken with 1, 9, 17, 33, and in the case of the 'aligned model', 49 scattering holes drilled in the acrylic models. The scatterers were all in equivalent locations relative to the other models. For each data taking sequence, the scatterers were filled first with air and then with water.

A Fast Fourier Transform (FFT) was performed on each waveform. The effects of geometrical spreading and intrinsic attenuation were eliminated by diving the frequency distribution of each waveform by the frequency distribution of the waveform generated at the same azimuthal angle when no scatterers were present. This spectral ratio shows the effects of the apparent attenuation. Finally, a systematic running average of each waveform was calculated to reduce the effects of noise and enhance the macroscopic trends in the waveforms.

RESULTS

Figures 1 and 2 are examples of coda for our receivers. Figure 1 shows the energy arriving at different times using the circular model with 33 scatterers. Figure 2 shows the a energy time plot from the circular model with no scatterers. This wave shows minimal coda.

An unusual "double dip" was observed in the spectral ratio plots for the circular model with water filled scatterers (Figure 3). These dips were not observed in plots of the air filled scatterers. Compressional waves to travel through the water in the scatterers. As compressional waves do travel through water, we speculate that the dips result from the effects of interference caused by the scatterers. The velocity of sound in water and acrylic

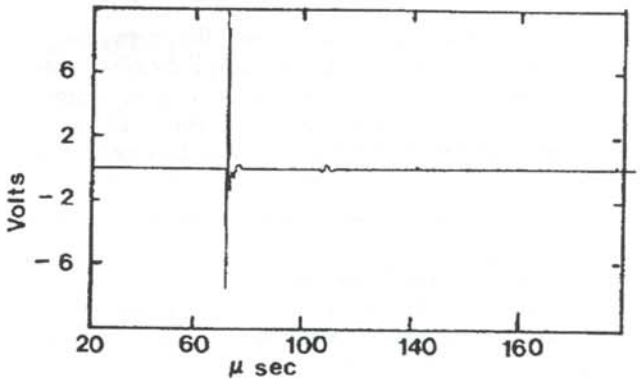

Figure 2

Voltage from the receiver vs time for a compressional wave with minimal coda. These data were collected from the circular model with no scatterers.

differ. The sound traveling through the acrylic with water filled scatterers should be slower than a corresponding wave propagating through the acrylic with no scatterers. When these waves reach the receiver transducer, they should be out of phase by an angle ϕ:

$$\phi = 2\pi f d\left(\frac{1}{v_w} - \frac{1}{v_a}\right), \qquad (1)$$

where d is the effective length of the scatterers (3 mm), $v_m = 1.5$ mm/μs (the velocity of sound in water), $v_a = 2.7$ mm/μs (the velocity of sound in acrylic) and f is the interference frequency. For destructive interference, the phase angle must be $(2n + 1)\pi$, $n = 0,1,2...$ The first minimum occur at frequency $f = 0.56$ MHz, which also corresponds closely with the graphs shown in Figure 3.

Figure 4 shows the spectral ratio for the aligned model at 90°. Again applying Equation 1 and estimating an effective length of 1 mm, the frequency of the first minimum is, coincidentally, 1.69 MHz, again corresponding to what is seen in Figure 4. The interference patterns are also seen when the number of scattering centers are increased. The interference effects were not seen in the data taken when air filled the scattering centers. This is due to the fact that an air filled scatterer causes total reflection of the wave, while the water filled scatterer permits some transmission of the incident wave.

The second minimum in Figure 3 is the second minimum as a result of interference, which coincidentally should exist at 1.69 MHz (a quick examination of the equation shows this is true). The initial dip in Figure 4 is not significant. It is the result of the limited responsiveness of the transducers at frequencies lower than about 0.4 MHz. In particular, the spectral ratios are high in this region because the scattering centers tend to produce lower frequency waves (this can be seen in Figure 1 as the coda). However, due to the limitations of the transducer and the lack of low frequency data from the waveforms with no scattering centers (Figure 2), quantifying this results is not meaningful

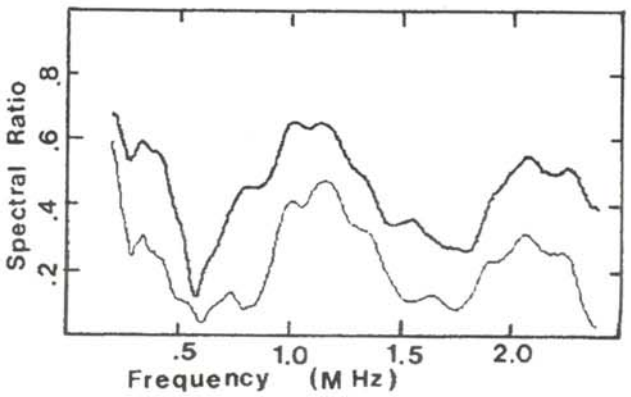

Figure 3
Spectral ratio as a function of frequency for the circular model filled with water showing interference. Bold line: 0° with 17 scatterers; normal line: 0° with 33 scatterers.

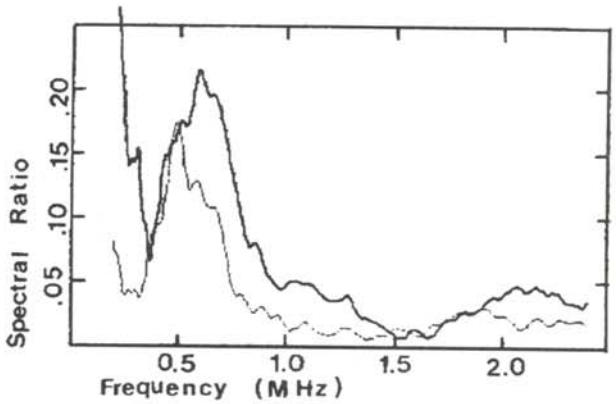

Figure 4
Spectral ratio vs frequency for the aligned model filled with water illustrating interference. Bold: 0°, 33 scatterers; Normal: 0°, 49 scatterers.

To determine the effect of the various types, distributions and contents of scatterers, we determined the attenuation factor, F, the ratio of the amplitude of the original waveform to the associated waveforms with scatterers. Figure 5 shows the behavior of F as the azimuthal angle is changed. The data were collected from the aligned model with 17 scattering centers. The water filled data shows interesting behavior at 67.5°. Figures 6 and 7 are the values of F as a function of azimuthal angle and number of scatterers.

In general, the attenuation factors increase as the azimuthal angle increases (up to 90°) and as the number of scatterers increases. [3] Figure 7, the values of F for water filled scatterers, shows that the attenuation factor is greatly reduced when the scatterers are filled with water. To interpret these results further would require a more definite understanding of the effects of impedance contrasts and the proximity of the scatterers to both the transmitting and receiving transducers. [4]

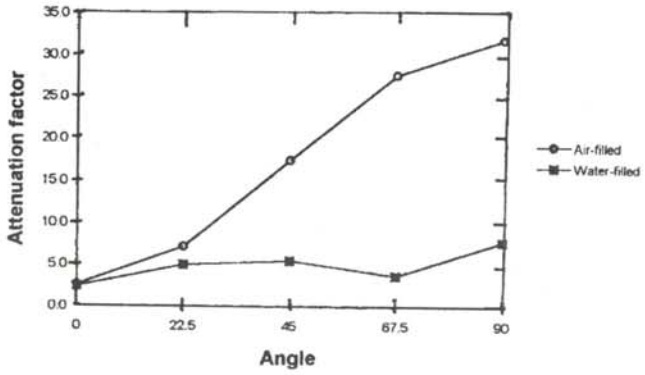

Figure 5
Attenuation factor vs scattering angle for 17 scatterers. The air filled scattering centers show a much higher attenuation factor. The water filled data shows interesting behavior at 67.5°

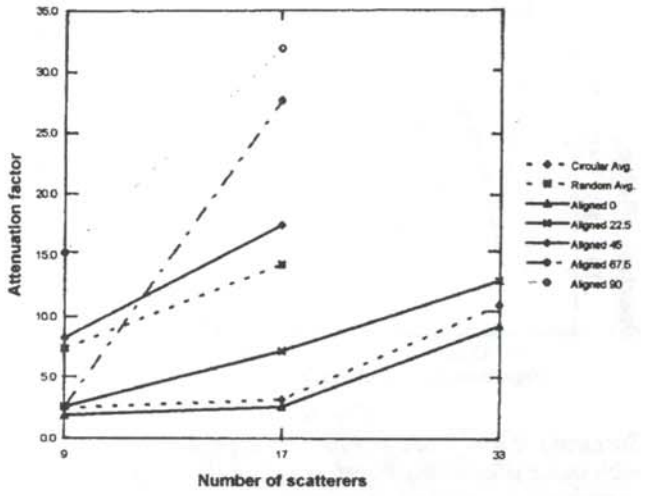

Figure 6
Attenuation factors for the aligned model with air-filled scatterers. Azimuthal angles from 0° to 90° are shown.

ACKNOWLEDGMENTS

The author would like to thank Dr. Bruce Dubendorff for his sponsorship ship of this research and for his assistance in the production of this paper. The research was funded by the Woods Research Grant through the Stetson University Seismo-Acoustic Laboratory.

REFERENCES

* current address of the author: 1323 W. Columbia Avenue, Apt. 1W. Chicago, IL 60626.

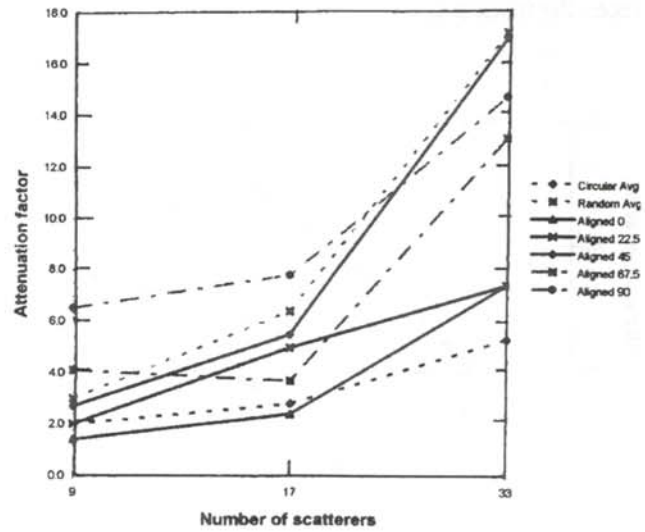

Figure 7
Attenuation factors for the aligned model with water filled scatterers. Azimuthal angles from 0° to 90° are shown.

1. For a more detailed discussion of physical model studies, techniques and applications, see : "Seismology: Physical Model Studies", The Encyclopedia of Solid Earth Geophysics, New York, Van Nostrand Reinhold Co., (1989), pp. 1202-1211.
2. Pulse-receiver : Panametrics model 505JPR, function generator : PASCO model PI-9587A
3. Data for 49 scatterers were discarded due to the uncertainty as to its validity. We were not able to isolate the initial pulse because of the large amount of attenuation.
4. A discussion of impedance contrasts can be found in Telford, et.al., Applied Geophysics, New York, Cambridge University Press, (1976), pp. 251-252.

FACULTY SPONSOR

Dr. Bruce Dubendorff
Department of Physics
Stetson University
DeLand, FL 32720

DFFICULTIES WITH RAYLEIGH SCATTERING AND FURTHER EXPLANATIONS FOR THE BLUIENESS OF THE SKY

Leslie Hsu*
Physics Department
University of Massachusetts Dartmouth
North Dartmouth, MA 02747
received April 2, 1995

ABSTRACT

The usual explanation for the blue color of the sky is based on Rayleigh scattering. What most physics books do not fully explain is why Rayleigh scattering does not make the sky look violet instead of blue. Experiments with a spectrometer and rotating Newton color disks show that the mixing of colors by the eye and brain as well as the range of spectral wavelengths that we detect as colors make us perceive the spectrum of the sky as a blue color.

INTRODUCTION

The colors of the sky have been studied and investigated for hundreds of years. At this point, the most important parts of this theory of the color of the sky are the principle of Rayleigh scattering and wavelength dependent sensitivity of the human eye. Some experiments have been performed to find out about the color of the sky. Leonardo da Vinci, over 400 years ago [1], observed the blue color produced when rays of sunlight fell on smoke or a fine spray of water and concluded that the same effect occurred in the atmosphere with sunlight and small particles of moisture. About three centuries later, in 1893, the British physicist John Tyndall did more experiments on the topic. [2] He passed a beam of white light through artificially produced smog and observed the color produced by the scattered light. Usually the light was milky white, but when the particles in the smog were especially small, the light turned blue. It wasn't until the late 1800's that physicist Lord Rayleigh unraveled the primary answer that is used to explain the blue sky. [3] He showed mathematically that particles with a diameter less than one tenth the wavelength of light would scatter the short wavelengths (blue) much more probably than the long wavelengths (red).

Leslie will enter Harvard University in the fall of 1996. This on going research was started in the spring of 1994 and has been successful in many state and national competitions. In her spare time, she enjoys playing the piano and basketball. She plants to concentrate in both physics and Earth sciences.

$$\sigma = \sigma_o \frac{1}{\lambda^4} \quad , \qquad (1)$$

where σ tells the probability of scattering, σ_o is a constant that depends upon the size of the particles doing the scattering and λ is the wavelength of the scattered light. This scattering law, that predicts that the scattering is proportional to the inverse fourth power of the wavelength, is the main explanation for the blue color of the sky in many existing physics text books and articles. [5]

When we speak of colors in this paper, such as the color blue, we are talking about a 'pure blue', the color that we see in the spectrum. There is a particular wavelength range that we perceive as blue. The range of wavelengths corresponding to a color differs. The differences in wavelength range are apparent when you look at a spectrum of sun light. Some of the wavelengths, such as red, are found in a wide band, while others, such as orange, are hard to distinguish.

The 'pure blue' is not to be confused with most blues that we see every day around us which are really mixtures of many different wavelengths. These colors are perceived as blue because of the way that our eyes and brain work together to mix the wavelengths and see a particular color.

In 'pure colors' violet and indigo have shorter wavelengths than those corresponding to blue. If Rayleigh scattering is the cause of the color of the sky, why isn't it violet instead of blue?

Some texts argue that the insensitivity of the eye to violet and indigo causes us not to see them even though they are present in great amounts in the sky. When we looked at

the sky with a spectrometer that used the eye as a detector, the spectrum clearly included violet and indigo as well as blue and green. Since we can see these wavelengths through a spectrometer, the insensitivity of our eye cannot be the explanation as to why the sky is blue.

Perhaps the apparent color of the sky is determined by the mixing of the colors. The reader should recall that the mixing of light and the mixing of pigments are quite different. If all the colors of light in the spectrum are combined, the result is white light. If all the pigments that correspond to colors in the spectrum are mixed together, the result is quite different. The difference is that light mixing is additive while pigment mixing is subtractive.

THE EXPERIMENT

In the mixing of light, there are a number of possible combinations of colors that can be called the *primary* colors. We will use the conventional (and most known system that is used by the TV industry) that includes red, green and blue-violet as the primary colors. In this system, the combination of red and blue-violet produces magenta, of green and red produces yellow, and of *blue-violet and green produces cyan - the color of the sky.* Since the green-blue-violet end of the spectrum is scattered by the small particles in the atmosphere in great amounts, the blue-violet and green primary colors can be mixed to produce cyan. This, along with the blue light already scattered, would make the abundance of the scattered light in the sky a blue hue.

To demonstrate the significance of the wavelength range and the mixing of colors, we developed some rotating Newton color disks. The real spectrum is a continuous distribution of colors and hues, but for simplicity (and due to convention), the seven colors: red, orange, yellow, green, blue, indigo and violet were used on the disks. Each color was arranged on the disk in a manner similar to a pie chart. The area of each slice corresponded to the amount of each color scattered. When the disk was spun at approximately 3500 rpm (as measured by a stroboscope) using a small motor, the colors mixed and a single color was produced. This process simulated the mixing of scattered light in the atmosphere to give us one perceptible color.

We made two types of disks: *set A* where only Rayleigh scattering was used to determine the proportions of the colors; *set B* which also took into account the wavelength range of the various colors and the solar spectrum. Equation 1 was used to decide the areas of the various disks of *set A*. The different disks in *set A* had different shades of the fundamental colors.

To make the disks in *set B*, we had to obtain the wavelength readings for different colors in the spectrum. The wavelength ranges of the spectrum, shown in Table 1, depend upon which source is used. We decided to use the Chambers Encyclopedia values because they included a range for indigo. We also included a factor to account for the fact that the violet end of the solar spectrum drops off.

When the disks of *set A* were spun, they generated a shade of violet. The spinning disks of *set B* all produced shades of blue. These results were independent of the shades of the various colors used in manufacturing the disks.

DISCUSSION

The apparent blue color of the sky is caused by a combination of effects. Rayleigh scattering causes the light to bend into our eyes and determines the 'pure colors' in the spectrum. The range of wavelengths that we perceive as specific colors and the way that our eye and brain mix the perceived colors change the sky from violet to blue.

In a sense, the behavior of the eye does indeed determine the color of the sky. It is not that the eye is most sensitive to green light and very insensitive to violet and red as is argued in some texts, but that the eye and brain have an interesting way of perceiving colors from the stimulations of the various wavelengths of light that hit it.

ACKNOWLEDGMENTS

The author would like to thank the faculty in the physics department at the University of Massachusetts Dartmouth for helpful discussions.

REFERENCES

* Current address of the author: 147 Lexington Avenue, North Dartmouth, MA 02747-3233.

	Range of Wavelengths in Ångstroms		
	Britannica[6]	Chambers[7]	Spectrometer[8]
Red	7600	7000	7600
Orange	6500	6050	6880
Yellow	6300	5950	6480
Green	4600	5800	6280
Blue	5000	5000	5200
Indigo	4200	4800	4760
Violet	----	4350	4560
	4000	4000	4000

Table 1

A list of the wavelength boundaries for each of the colors. These values were used in calculations of the areas for each section of the Newton color disks.

1. Jean-Paul Richter, The Literary Works of Leonardo da Vinci, Oxford University Press, London, (1939), pp. 237-240.
2. L.D. La Mer and Milton Kerker, "Light Scattered by Particles," Sci. Amer., (Feb 1953), pp. 69-76.
3. Lord Rayleigh, W.L. Bragg and G. Porter, The Royal Institution Library of Science : Physical Sciences, Elsevier, New York, (1970), Vol 8, pp: 309-317.
4. One point that is mentioned very sparsely in the texts is Mie scattering. In the atmosphere, there are many particles beside the small air molecules that scatter the sunlight. Certain larger particles will scatter the sun light according to Mie's theory, which explains the scattering by a uniform sphere. This theory was not developed as a result of studying the sky's colors, as was Rayleigh's law, but it still applies to the problem related to the blue sky. For example, see "Scattering by a Uniform Sphere (Mie Theory)" in R.B. Newton, Scattering Theory of Waves and Particles, McGraw-Hill, New York, (1966), pp. 47-51 and the references in that article.
5. See, for example, J.J. Sakurai, Advanced Quantum Mechanics, Addison-Wesley, Reading, MA, (1967), p. 51; V.F. Weisskopf, Sci. Amer. 219, 3, (Sept 1968), p. 61; V.F. Weisskopf, Physics of the Twentieth Century, MIT Press, Cambridge, (1972), p. 254; W.T. Grandy, Jr. Introduction to Electrodynamics and Radiation, Academic Press, Inc., New York (1970), p. 359; W.K.H. Panofsky and M. Phillips, Classical Electricity and Magnetism, Addison-Wesley, Reading, MA, (1962), p. 407; J. Walker, Sci. Amer., (Jan 1989), pp. 102-205.; J. Walker, The Flying Circus of Physics, with Answers, John Wiley and Sons, New York, (1977), p. 130, 274.
6. Encyclopedia Britannica, Vol III, (1980), pp. 22-23.
7. Chamber's Encyclopedia, Vol IV, 1967, p. 751
8. These wavelengths were obtained by looking at the sun with a grating spectrometer that had degree markings on it. From the recorded markings, the relative proportions of the wavelength ranges could be calculated. The range of angles for a color is proportional to the wavelength range rather than the frequency range because the angle of diffraction of a grating is approximately linearly related to the wavelength. The range of wavelengths may be pictured as proportional to the number of photons of a specific color.

FACULTY SPONSOR

Professor Jong-Ping Hsu
Physics Department
University of Massachusetts Dartmouth
North Dartmouth, MA 02747-2300

ATOMIC STRUCTURE OF NIOBIUM CARBIDE (100) AND (110) SURFACES STUDIED BY SCANNING TUNNELING MICROSCOPY

Ralph M. Tsong
Physics Department
The College of William and Mary
Williamsburg, VA 23186
received September 12, 1995

ABSTRACT

The surfaces of $NbC_{0.75}$ (100) and $NbC_{0.865}$ (110) single crystals were studied using an ultrahigh vacuum scanning tunneling microscope (STM) with in situ cleaning facilities of sputtering and annealing. STM images show atom resolved structures on both surfaces. On $NbC_{0.75}$ (100), a square (1x1) served, together with regions of hexagonal structure, indicative of a different surface phase, possibly that of Nb_4C_{3-x}. On $NbC_{0.865}$ (110), a faceted surface was observed with a (nx1) structure, where n is 4 or 5. The atom resolved images were most probably due to the Nb atoms while the C atoms were not imaged.

INTRODUCTION

Transition metal carbides have been of considerable technological interest in the past three decades because of their unusual combination of physical properties: high melting points; good electrical conductivity and extreme hardness. They are almost always non-stoichiometric, containing vacancies in the carbon lattice sites with a range of compositions. In the present report, the carbides of interest are single crystals of NbC (100) and NbC (110). These carbides possess a single crystal structure of the NaCl type as shown in Figure 1. The lattice parameter of NbC is 4.43Å [1], corresponding to the length of an edge of the cube shown in Figure 1. This means that the closest Nb-Nb and C-C distance is 3.13Å. The ideal bulk-terminated (1x1) surfaces of NbC (110) and NbC (110) are shown schematically in Figure 2(a) and (b) respectively.

Little work has been previously done to determine the surface structures of NbC (100) and NbC (110). Researchers from Japan [3,4] have reported gas adsorption studies on NbC (100), while a group from Oak Ridge National Laboratory has determined the structures of (100) surfaces of related carbides of TaC and HfC using the technique of low energy electron-diffraction (LEED). [5,6]

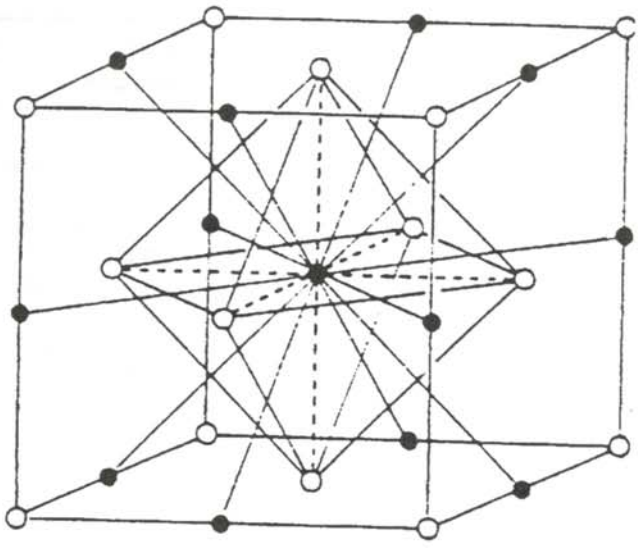

Figure 1
Schematic cubic unit cell of NbC. Open circles represent Nb atoms at the fcc positions and filled circles represent C atoms at octahedral intersitial sites. The structure is the same as that of NaCl.

Ralph Tsong is a senior mathematics major and physics minor at the College of Willima and Mary. This research took place during the summer of 1995 at the Institut für Allgemeine Physik at the Technische Universität Wien, in Vienna, Austria, as part of his James Monroe Scholarship project. In his free time, he enjoys drawing cartoons, lrunning and going to clubs. He plans to attend law school after graduating.

There have been no reports of any investigation conducted on the NbC (110) surface. However, the surface structure of TaC (110) has been studied using scanning tunneling microscopy (STM). [7] A recent review of transition metal carbide and nitride surfaces has been presented. [8]

Despite the fact that numerous STM studies have been conducted on the surfaces of metals and semiconductors over the past decade, the only STM studies on transition metal carbide surfaces were the work on TaC (110) [7] and VC0.8 (111) [9]. This apparent lack of interest is likely due to the difficulty in producing a high quality clean and ordered surface of the carbide crystal.

THE EXPERIMENT

The NbC_{1-x} single crystals, where $1-x = 0.750$ for the (100) orientation and $1-x = 0.865$ for the (110) orientation, were grown by the floating zone method. The crystals were cut by spark erosion into 2 mm thick disks and polished mechanically. Details of preparation and chemical composition of these crystals can be found elsewhere. [10]

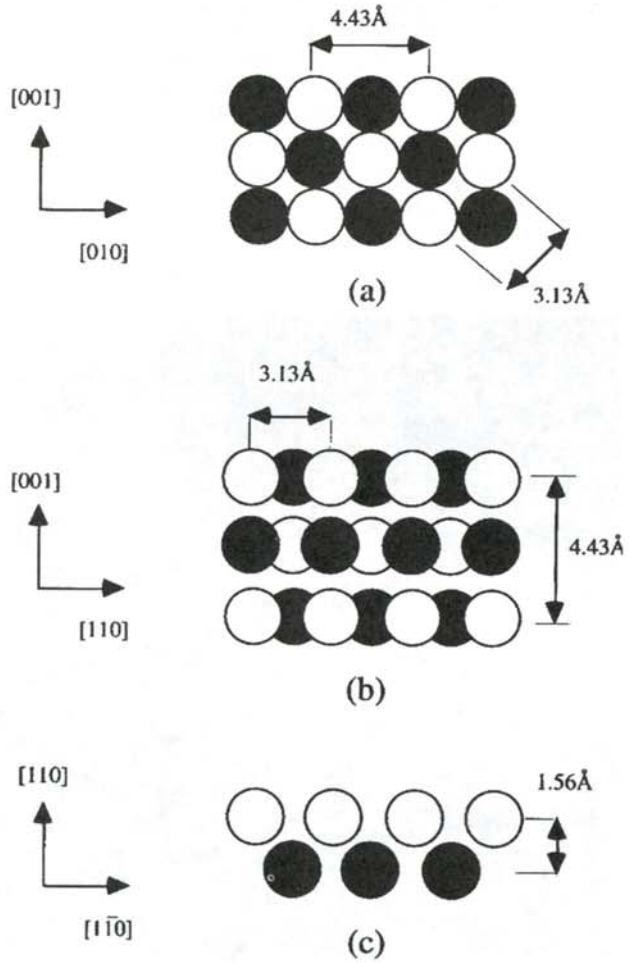

Figure 2
a) The top view of the (1x1) bulk terminated surface of NbC (100). The side view is identical. b) Top view and c) side view of the (1x1) surface of NbC(110). Open circles are Nb and filled circles are C atoms.

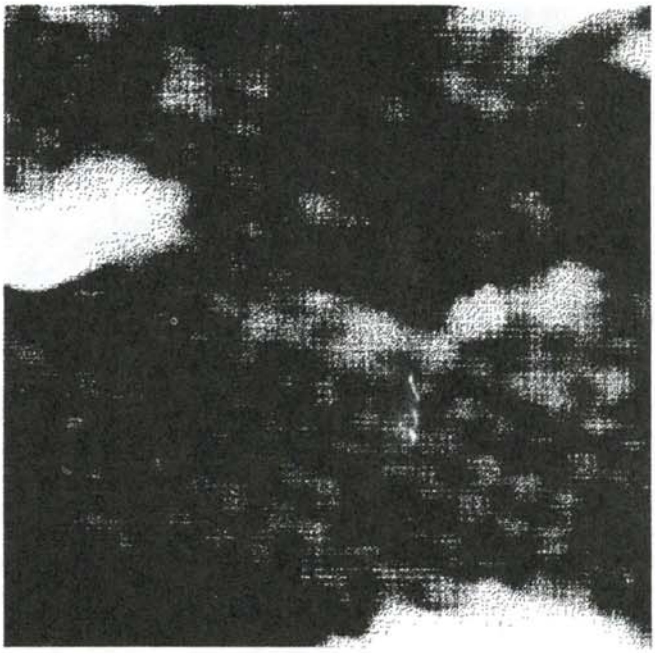

Figure 3
A 50Å x 50Å STM image of the $NbC_{0.75}$ (100) surface showing a square (1x1) geometry of the atoms. The distance between the two nearest atoms is 3.1 Å.

The ultrahigh vacuum scanning tunneling microscope (UHV-STM) apparatus consists of two interconnected chambers, one for sample preparation and the other for housing the STM. The $NbC_{0.75}$ (100) sample was installed into the preparation chamber at a pressure $\leq 2 \times 10^{-10}$ mbar, to undergo sputtering and annealing cycles to produce a clean and ordered surface before being examined by the STM. The surface was sputtered with 1 keV Ar^+ ions at an incident angle of 67° with an ion current of 1.5 μA for 10 minute periods. The sample was then annealed at temperatures ranging form 1000C to 1180C, also for 10 minute periods. We did not obtain an ordered LEED pattern after the sputtering and annealing cycles. [3,4] Auger electron spectroscopy (AES) scans of the surface showed that some oxygen remained.

The $NbC_{0.865}$ (110) sample was treated with similar cycles of sputtering and annealing between 1000C and 1150C. In this case, however, an ordered LEED pattern was observed with elongated spots indicative of a (4x1) or a (5x1) reconstruction after the cleaning treatment. No trace of oxygen contamination was detected by AES.

After the cleaning treatment, the samples were individually transferred from the preparation chamber to the STM chamber, maintaining the UHV. The pressure inside the STM chamber was typically below 1×10^{-10} mbar. Once

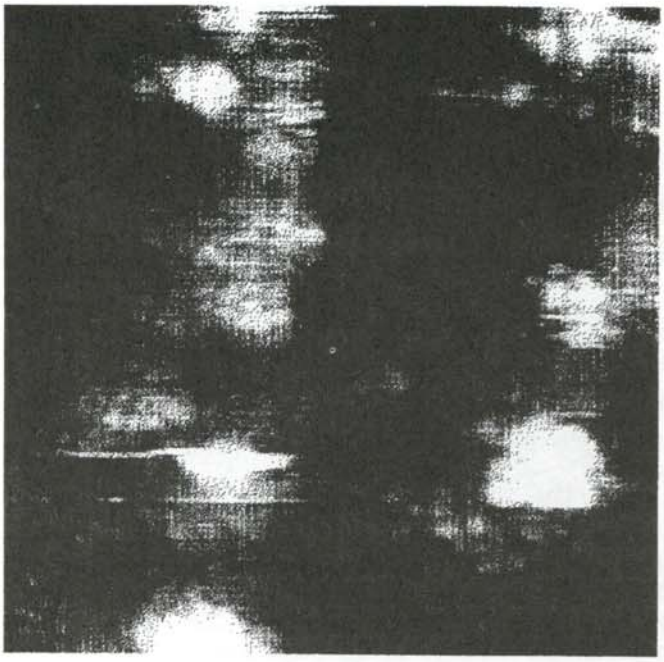

Figure 4
A 100Å x 100Å STM image of the $NbC_{0.75}$ (100) surface showing patches of hexagonal arrangement of atoms on the surface. The nearest neighbor distance in the hexagonal structure is 2.5Å.

the sample was mounted inside the STM, scanning was carried out with a gap voltage between 5 and 10 mV, with a negative bias on the sample and a tunneling current of ≈1 nA. Similar to other experiments on $VC_{0.8}$ [9], the tunneling voltage and current settings were not critical and reversing the bias had no noticeable affect on the image.

RESULTS AND DISCUSSION

$NbC_{0.75}$ (100)

The lack of any LEED pattern from the $NbC_{0.75}$ (100) surface after the cleaning treatment indicated that the surface did not have any long-range order. The STM images support this finding. Figure 3 shows an atom resolved STM image over a small region, 50Å x 50Å of the $NbC_{0.75}$ (100) surface. The bright spots form a square array with a spacing of 3.1Å between nearest neighbors. This corresponds to the (1x1) bulk terminated surface shown in Figures 2a, with only one of the atom species present. It is likely that the Nb atoms were imaged in Figure 3 because there are no vacancies among the bright spots. The carbon in $NbC_{0.75}$ is under stoichiometric, i.e $(1-x) < 1$, in NbC_{1-x}. Thus, we would expect to find ≈25% vacancies among the bright spots if carbon atoms were imaged.

On other parts of the (100) surface, STM images show bright spots arranged in a hexagonal pattern with nearest neighbor distances of 2.5Å. Such an image is shown in Figure 4. This somewhat disordered hexagonal surface phase coexists with the (1x1) phase shown in Figure 3. The coexistence of these two phases, plus other disordered regions on the surface contribute to the absence of a LEED pattern on the (100) surface. The hexagonal structure could be the result of a transitional phase below 1800C between 40 and 42 atomic percent of carbon in the NbC phase diagram. [11] Since the $NbC_{0.75}$ has 42.86% carbon, the cleaning treatment of sputtering and annealing cycles could conceivably lower the carbon content into the transitional phase. Carbon to niobium peak ratios from AES scans taken after each sputtering and annealing cycles indicated a diminishing trend of carbon, which may have been enough to change the carbon content to < 42% on the surface. The transitional phase between NbC_{1-x} and Nb_4C_{3-x} could possibly account for the hexagonal structure observed in Figure 4, although the exact structure of this phase has not been determined. [11]

$NbC_{0.865}$ (110)

STM images of $NbC_{0.865}$ (110) surface after the cleaning treatment show a ridge and valley grating structure, similar to that observed for the TaC (110) surface. [7] A typical STM image of this grating structure is shown in Figure 5. A high resolution image of the grating structure is displayed in Figure 6. The distance between two adjacent bright spots on the same row in Figure 6 is 4.5Å. Thus, according to Figure 2b, the spacing between two atom rows on the same plane must be multiples of a = 3.13Å, giving a (nx1) reconstruction on the surface. From the

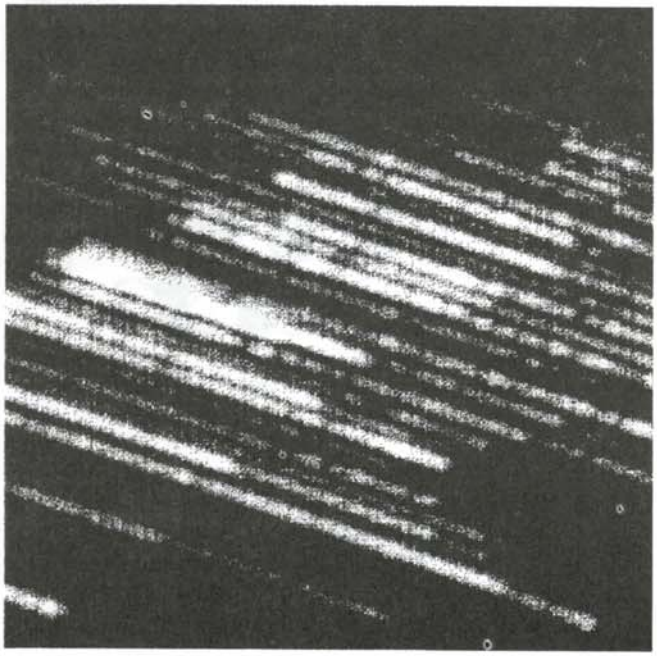

Figure 5
A 500Å x 500Å STM image of the $NbC_{0.865}$ (110) surface showing a ridge and valley grating (nx1) structure. The "1" direction lies along the ridges and the "n" direction across the ridges.

gray scale of Figure 6, we can identify three atom rows near the top of the image to be on the same plane, which we have labeled plane 1. The rows on plane 2 in Figure 6 are 1.56Å below plane 1. The adjacent atom rows on plane 1 are 16Å (or about 5a) apart. Adjacent atom rows on plane 2 in the top half of Figure 6 are 12.5Å (about 4a) apart. The two atom rows on plane 2 at the bottom half of Figure 6 are 16Å (about 5a) apart. The spacing between an atom row on plane 1 next to an atom row on plane 2 is 15Å (about 4.5a apart).

A model to explain our observations in Figure 6 is shown in Figure 7, where the atom rows run along the [001] direction, perpendicular to the plane of the paper. Atom rows on the same plane can have a spacing of 4a or 5a depending upon the depth of the valleys. Single line scans taken along the grating structure, such as that shown in Figure 5, reveal that the valley walls are (100) and (010) facets, as labelled in Figure 7. The orientations of the facets are similar to those reported for TaC. [7]

The question remains whether the bright rows in Figure 5 and the bright spots in Figure 6 are due to Nb or C atoms. From Figure 6, the measured spacing of 4.5Å between bright spots tells us that they are either Nb or C atoms, but not both. It is tempting to suggest that they are due to C atoms from the discontinuous nature of the rows observed in Figure 5, indicative perhaps of the carbon vacancies in the non-stoichiometric $NbC_{0.865}$. However, a careful examination of Figure 5 and other such images of the grating structure reveals that although some rows may be discontinuous on the same plane, they almost always continue to extend on a lower plane. We have never come across any rows in an image which are antiphase: an upper row straddling two lower rows, which could signal the true termination of a row. So, it is impossible to tell from Figures 5 and 6 whether the Nb or C atom is imaged by the STM on the (110) surface. We have, however, concluded earlier from Figure 3 for the (100) surface that Nb atoms were imaged by the STM. Moreover, a STM study of

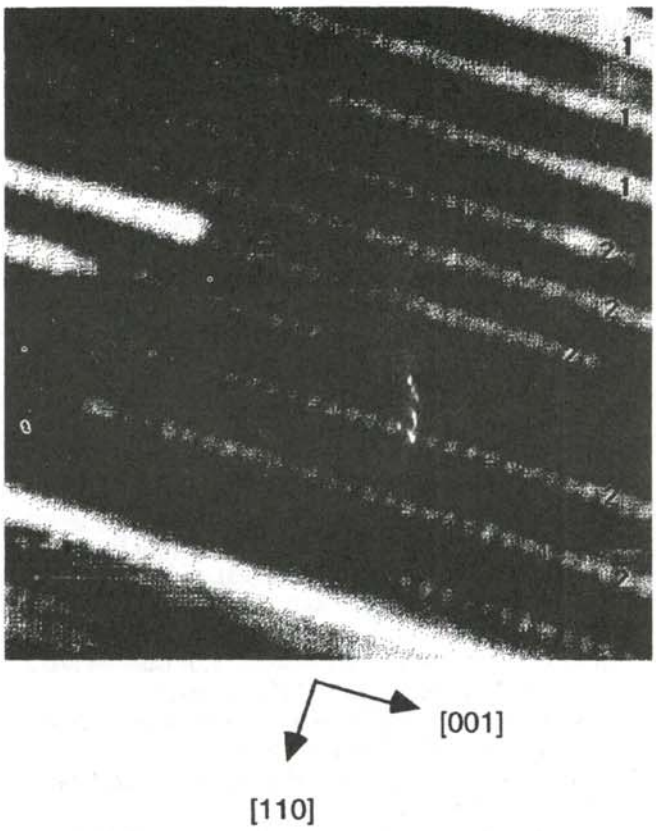

Figure 6
An atom resolved 150Å x 150Å STM image of the (nx1) grating structure. The distance between two adjacent atoms is 4.5Å, thus the atom rows or 'ridges' lie along the [001] direction. The rows marked '1' lie on the same plane, while those rows marked '2' lie on a plane 1.5Å below plane 1.

carbon segregation on a $Pt_{10}Ni_{90}$ (100) surface [12] showed that in general, only the metal atoms are imaged. The carbon atoms showed their presence only by lowering the apparent height of the neighboring metal atoms. Thus, the bright features in Figures 5 and 6 are most likely due to Nb atoms and not C atoms.

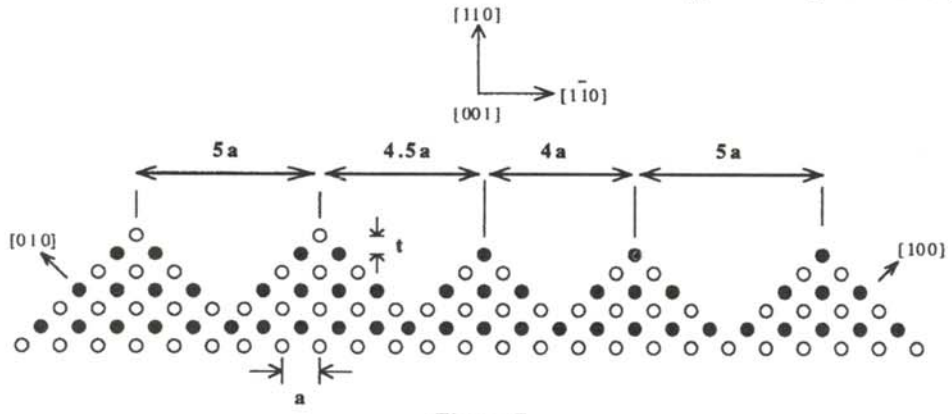

Figure 7
A schematic model showing the ridges and their spacings. Each ridge (or atom row) lies perpendicular to the paper in the [001] direction. a = 3.13Å and t = 1.56Å as defined in Figures 2. The facet directions of [100] and [010] are also shown.

ACKNOWLEDGMENTS
The author wishes to thank The College of William and Mary for the award of a James Monroe Scholarship to carry out this work in the UHV-STM laboratory at the Technische Universität Wien in Austria. He is grateful for the hospitality, guidance and assistance of Professor Peter Varga, Dr. Michael Schmid and Mr. Christian Nagl of the TU Wien during the course of

this work. The NbC crystals were kindly supplied by Professor Robert F. Davis of North Carolina State University.

REFERENCES

1. E.K. Storms, *The Refractory Carbides*, Academic Press, New York, (1967).
2. L.E. Toth, *Transition Metal Carbides and Nitrides*, Academic Press, New York, (1971).
3. I. Kojima, M. Orita, E. Miyazaki and S. Otami, Surf. Sci., 160, (1985), p. 153.
4. E. Edamoto, S. Maehama, E. Miyazaki, H. Kato and S. Otani, Surf. Sci., 223, (1989), p. 56.
5. J.R. Noonan, H.L. Davis and G.R. Gruzalski, J. Vac. Sci. Technol., A5, (1987), p. 787.
6. G.R. Gruzalski, D.M. Zehner, J.R. Noonan, H.L. Davis, R.A. Didio and K. Müller, J. Vac Sci. Technol., A7, (1989), p. 2054.
7. J.K. Zuo, R.J. Warmack, D.M. Zehner and J.F. Wendelken, Phys. Rev., B47, (1993), p. 10743.
8. L.I. Johansson, Surf. Sci. Rep., 21, (1995), P. 177.
9. M. Hammar, C. Törnevik, J. Rundgren, Y. Gauthier, S.A. Flodström, K.L. Håkansson, L.I. Johansson and J. Häglund, Phys. Rev., B45, (1992), p. 6118.
10. H.M. Ledbetter, S. Chevacharonekul and R.F. Davis, J. Appl. Phys., 60, (1986), p. 1614.
11. J.F. Smith, O.N. Carlson and R.R. DeAvillez, J. Nucl. Mat., 148, (1987), p. 1.
12. M. Schmid, A. Biedermann and P. Varga, Surf. Sci. Lett., 294, (1993), p. L952.

FACULTY SPONSOR

Professor Peter Varga
Institut für Allgemeine Physik
Technische Universität Wien
Wiedner Hauptstrasse 8 - 10/134
A-1040 Wien, Austria
Varga@eavp38.tuwien.ac.at

A FIRST PRINCIPLES INVESTIGATION OF POLYPEPTIDE NANOTUBES

Norma H. Pawley *
Department of Physics and Astronomy
Arizona State University
Tempe, AZ 85287-1504
received September 12, 1995

ABSTRACT

The complexity of biological systems has long deterred their investigation by *ab initio* methods. Several recent advances in theoretical techniques have made the study of large systems possible. This study presents the results of the first *ab initio* molecular dynamics simulation of polypeptide nanotubes. The calculations show that the cohesive energy of the ring changes as a function of internal diameter, with an eight residue ring being the optimal size. The energy band gap of the eight residue ring is large, making it a transparent insulator, in coincidence with experimental evidence. Hydrogen bonding is found to play an essential role in ring stability.

INTRODUCTION

Artificial structures of nanometer length scales, often referred to as nanotubes, have been the subject of much interest in recent years. Nanotubes can be formed from a variety of constituents, including organic material, such as polypeptide rings. These rings are formed when special combinations of amino acids are joined by a covalent bond, known as the peptide bond. Polypeptide nanotubes, formed by the stacking of polypeptide rings, have unique advantages in many applications. Possible applications range from drug-delivery systems to novel cytotoxic agents, from nano-scale test tubes to templates for circuit miniaturization [1,2]. Interest in these peptide nanotubes has increased sharply since 1993 with the discovery of a process for inducing self-assembly. [1]

Many important questions concerning the properties of these systems remain. The design of medical applications will require understanding the roles of hydrogen bonding, composition and tube diameter in self-assembly and stabilization. Information about the electronic structure, the vibrational modes and the bulk modulus will help determine the suitability of peptide nanotubes for applications in electronic and optical devices.

The properties of these tubes have not yet been studied using first principles (*ab initio*) techniques. First principles techniques involve finding solutions to Schrödinger's equation for a system. Until recently, *ab initio* calculations were far too computationally intensive to successfully treat large biological systems. In addition, a simple, yet accurate, *ab initio* theory describing hydrogen bonding interactions, which play a critical role in

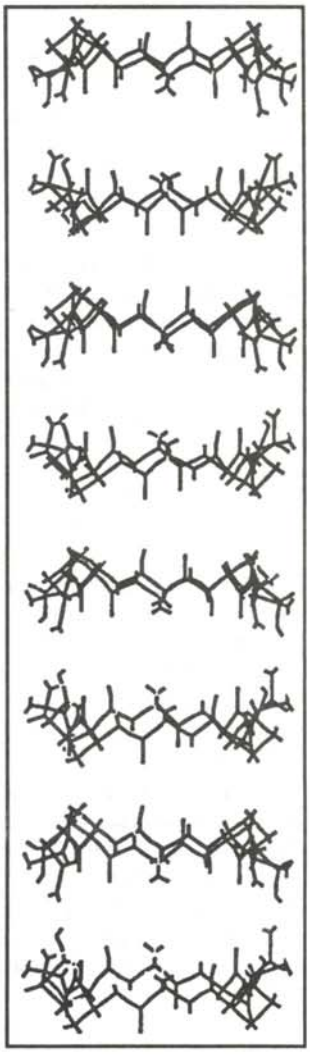

Figure 1
Theoretical image of a nanotube built from individual cyclic peptide rings that are hydrogen bonded together.

Norma is a senior physics major at the Colorado School of Mines. This research was begun during the summer after her junior year when she worked as part of an NSF sponsored research program at Arizona State University. In her spare time, she enjoys mountain climbing and windsurfing. She is planning to attend graduate school in biophysics in the fall.

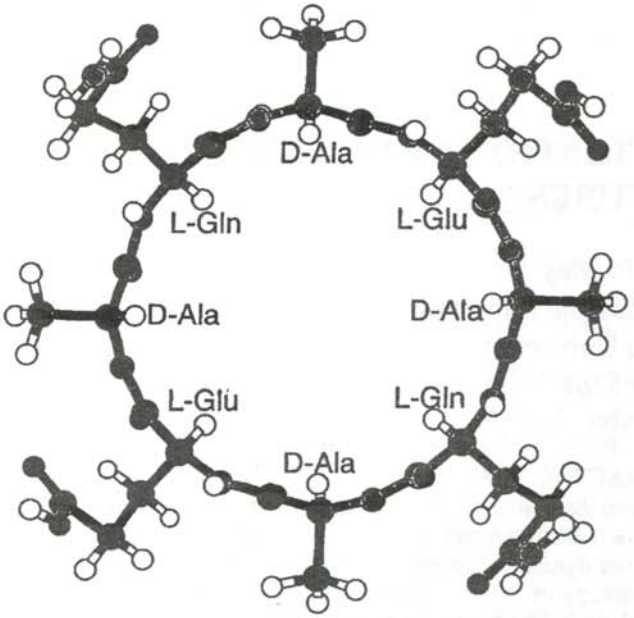

Figure 2
Polypeptide ring, [(D-Ala-Glu-D-Ala-Gln)$_2$], composed of eight amino acids. This ring size is the most energetically favorable. When AMBER is used with bond angle constraints in place, a ring shape, much like the image shown, is obtained. The image was produced using Xmol.

biological functions, was necessary. Such a theory has only recently been developed.

HISTORICAL BACKGROUND

According to a theory first advanced in 1973, alternating the chirality of amino acids in a polypeptide chain could cause the molecule to adopt a flat ring shaped conformation. [3] The rings could then interact through hydrogen bonding in antiparallel beta sheet folding to form vertically stacked beta barrels or nanotubes similar to Figure 1. Since 1973, the proposed structures have been investigated both experimentally [4-8] and theoretically [9,10]. Interest, however, remained sporadic until 1993.

In 1993, it was discovered that controlled acidification of alkaline peptide solutions triggered the spontaneous self assembly of hundreds of tightly packed nanotubes. [1] In 1994, the same group demonstrated that these molecules will self assemble not only in solution, but also in a lipid bilayer. Assembly in lipid bilayers opens avenues for application as artificial transmembrane ion channels that mimic the biological function of natural compounds. [2] Additional research has shown that these tubes make excellent channels for transport across membranes of not only ions, but also glucose. [11]. This is unexpected since the Coulomb forces between a glucose molecule and a nanotube are much smaller than the Coulomb forces between an ion and a nanotube.

The nanotube structures assembled and identified by Ghadiri et.al. [1] are composed of alternating amino acid residues, the simplest of which is the cyclic octapeptide, [(D-Ala-Glu-D-Ala-Gin)$_2$], shown in Figure 2. The ring structure has an internal diameter of 7-8 Å and the tubes can be up to several hundred Å long. Larger rings have been created, forming tubes with an internal diameter up to 13 Å. In addition, the residues have been varied to produce tubes with distinctive characteristics [1,11,12].

This study explores the stability of a single ring composed of 8 amino acid residues, as shown in Figure 2, and calculates the electronic density of states for this structure. Other polypeptides derived from the basic formula [(D-Ala-Glu-D-Ala-Gin)$_m$] were also investigated. The parameter m was varied from 1 to 4. The remaining rings are shown in Figures 3,4, and 5, corresponding to m = 1,3, and 4 respectively. For each structure, the total energy of the optimized configuration was computed.

COMPUTATIONAL METHODS

In the 1960's, quantum chemistry was expected to be capable of solving any electronic structure problem using first principles methods. For biological systems, this expectation has remained largely unfulfilled. The main reason for this failure has been the computational intensity required for quantum chemistry calculations of many atom systems with complex geometries. Hartree-Fock calculations, for example, scale as N^4, where N is proportional to the number of atoms in the system. A series of recent theoretical advances, however, have made larger systems tractable by *ab initio* methods.

Many of these developments rely on the use of a linear combination of atomic orbitals (LCAO) approach for their computational speed. The LCAO, or tight binding

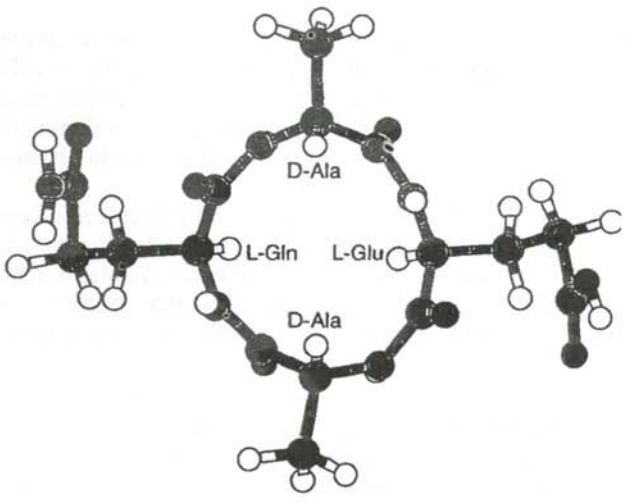

Figure 3
Polypeptide ring, [(D-Ala-Glu-D-Ala-Gln)$_1$], composed of 4 amino acids. This ring is the least energetically favorable. Distorted bond angles contribute to a higher energy configuration. The image was produced using Xmol.

method, does not treat electrons as infinitely extended plane waves as in the Hartree-Fock approximation. Instead, each electron is treated as localized around a nucleus and interacting with a limited number of neighbors. A further advance in computational speed occurs when the LCAO is combined with the local density approximation (LDA). [13,14] Details of such a combination can be found elsewhere. [15] Still, the computational time scales as N^3. Such an improvement is only sufficient for treating systems of up to 100 atoms; large biological molecules far exceed computational capabilities.

Recently, order N methods have been successfully developed. [16-21] With order N approximations, when the number of atoms in a molecule is tripled, the time necessary for calculations simply triples rather than increasing by a factor of 27 or 81. This linear scaling makes the computational efficiency of electronic structure calculations sufficient for the study of biological macromolecules.

Computational time was not the only challenge involved in the study of biological molecules. Another major advance necessary for a complete treatment of biological systems was the development of a theory for accurately, yet simply, determining the microscopic effects of the hydrogen bond. The development of a hydrogen bonding theory using the LCAO formalism and its successful application to the test case of H_2O has been recently reported. [22] This method has subsequently been applied to the much more challenging problem of interactions between DNA base pairs and triplets. [23]

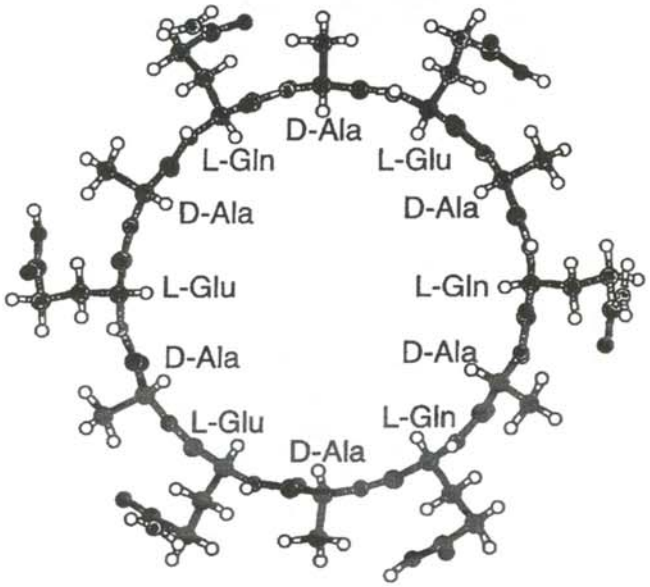

Figure 4
Polypeptide ring, [(D-Ala-Glu-D-Ala-Gln)$_3$], composed of 12 amino acids. Although higher in energy than the 8 residue ring, tubes of this size have been experimentally produced. The image was produced using Xmol.

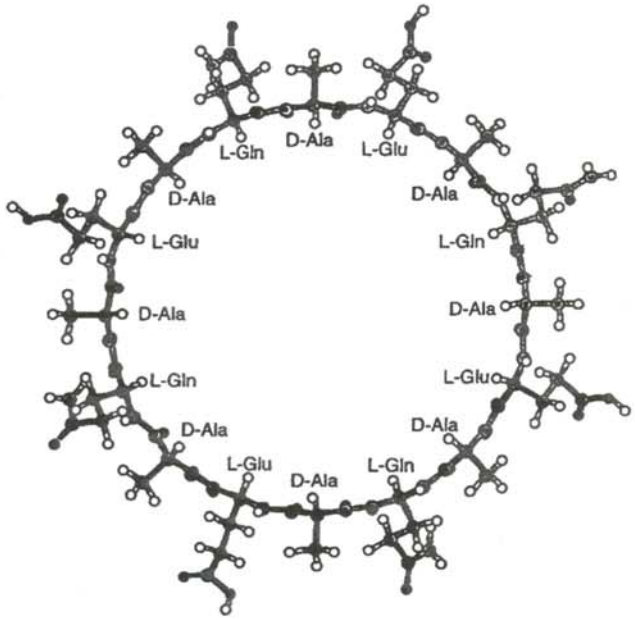

Figure 5
Polypeptide ring, [(D-Ala-Glu-D-Ala-Gln)$_4$], composed of 16 amino acids. Calculations show that this structure has the same minimum energy as the 12 residue ring. The image was produced using Xmol.

Using the techniques described above, the total energy of large biological molecules, such as polypeptide rings, can be found. Once the total energy as a function of atomic position is known, the forces on the atoms can be calculated. This is accomplished using the Hellmann-Feynman theorem. [24,25] The force on an atom, j, due to another atom, i, can be obtained by taking the derivative of the total energy, E_{tot}, with respect to the distance from atom i to atom j, r_j.

$$\vec{F}_j = -\frac{\partial E_{tot}}{\partial \vec{r}_j} \qquad (1)$$

Then quantum molecular dynamics simulations can be performed using the calculated forces.

A dynamical quenching process is used to determine the minimum energy geometric configuration. In this process, the equations of motion of each atom are solved and the resulting total kinetic energy, KE_{tot}:

$$KE_{tot} = \sum_j \frac{1}{2} m_j v_j^2 \qquad (2)$$

When the kinetic energy reaches a maximum, the potential energy must be at a local minimum. At this point, the velocities are quenched (set equal to 0). This process is repeated until the forces on each atom are zero within a given tolerance.

A commercial program for the interactive display and simulation of molecules was used to build the basic structures. In an effort to obtain a good starting basis for

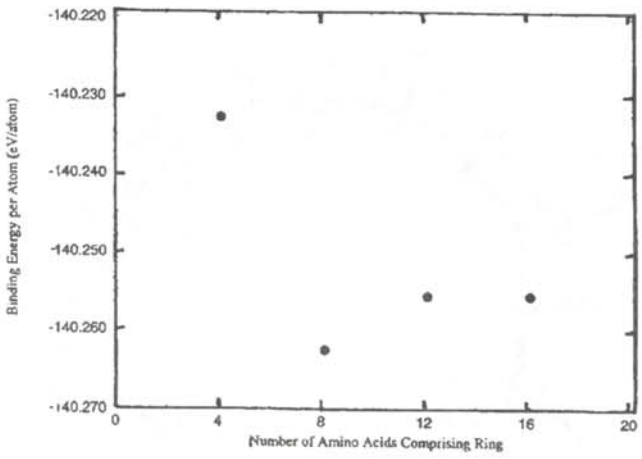

Figure 6
Binding energy per atom of minimum energy configurations for the four polypeptide rings. This plot shows that the [(D-Ala-Glu-D-Ala-Gln)$_2$] structure is the most energetically favorable.

the *ab initio* calculations, the structures were first allowed to fall to their minimum energy configuration under classical potentials using the AMBER [27] program that allows structures to be formed with special constraints on the form of the molecule. Calculations were performed on structures formed by AMBER both with and without these constraints. The *ab initio* calculations were performed without special constraints.

RESULTS

Energy as a Function of Ring Size

The graph in Figure 6 shows the total energy per atom as a function of the number of residues composing the ring for the four [(D-Ala-Glu-D-Ala-Gin)$_m$] structures (with m = 1,2,3 and 4. The most favorable ring size is the eight residue ring. For rings composed of twelve residues or more, the cohesive energy remains constant.

An examination of the bond angles on the main ring show a pattern to these results. The atoms that form the main ring undergo either sp^2 or sp^3 hybridization. Ideally, the sp^2 bond angle is 120° and the sp^3 bond angle is 109°. The 4 residue ring has the largest sp^3 bond angle deviation from ideal, an average bond angle of 101°. The distortion of these angles is significant enough to be visible in Figure 3. The 4 residue ring also has the highest cohesive energy. The 8, 12 and 16 residue rings have sp^3 deviations that are nearly the same, averaging around 104.5°. These values are closer to the ideal bond angle. For these rings, the sp^2 bond angle deviations are more significant. The 8 residue ring has the smallest deviations from the ideal sp^2 bond angles, and it is also the most energetically favorable structure. The 12 and 16 residue rings have sp^2 bond angle deviations that are nearly the same. These two ring sizes also have nearly the same energy. Although the 8 residue ring has the minimum energy, experimentalists have seen tubes of 12 residue rings self-assemble. Our results imply that based on energetics alone, attempts to build 16 residue rings and larger should be equally successful. Entropy effects, however, will likely limit the number of residues composing the rings.

Electronic Density of States

The electronic density of states was obtained from the energy eigenvalues of the Schrödinger equation. The density of states for the eight residue ring is shown in Figure 7. The quantity E_{HL} represents the difference in energy between the highest occupied molecular orbital and the lowest unoccupied molecular orbital. This energy gap is 4.66 eV. For comparison, the energy gap for the diamond form silicon semiconductor is 1.17 eV, the gap for the ordered silicon-carbide semiconductor is 2.39 eV and the gap for the carbon diamond insulator is 5.5 eV. The single octapeptide ring is clearly a wide gap insulator. The energy of visible light ranges from 1.8 eV to 3.1 eV. Therefore, a gap of 4.66 eV indicates that the ring is transparent. The nanotube samples obtained by Ghadiri *et al.* were reported as colorless prismatic crystals. [26]

Stability and the Role of Hydrogen Bonding

The initial configuration for all the investigated structures was obtained using the AMBER program. This program produced two possible shapes for the same polypeptide sequence. Both possible shapes of the 8 residue polypeptide were studied using electronic structure techniques to determine which shape was more energetically favorable.

The first shape is shown in Figure 2. This structure was relaxed with constraints on all bond angles which forced AMBER to maintain the ring shape in the first step. *Ab initio* calculations were then performed with no constraints, allowing the molecule to choose its own minimum

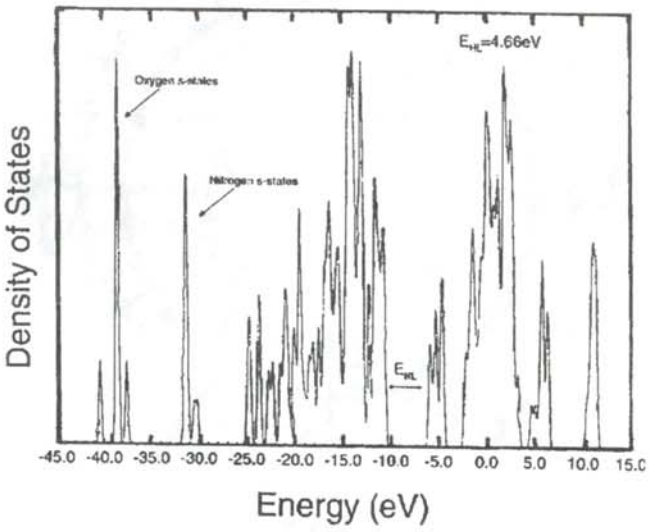

Figure 7
Electronic density of states of the cyclic octapeptide [(D-Ala-Glu-D-Ala-Gln)$_2$]. The energy gap of 4.66 eV indicates that the molecule is a transparent insulator.

energy configuration. The molecule relaxed to its minimum energy configuration maintaining the ring shape in every molecular dynamics step.

The second shape is shown in Figure 8. This structure was relaxed without constraints on the bond angles. Thus, AMBER was not forced to maintain the ring shape. In this case, the molecule distorted to the shape shown in Figure 8. *Ab initio* calculations were used to find a minimum energy configuration for this structure as well.

Surprisingly, the *ab initio* calculations show that the two structures, though very different in appearance and achieved by different methods, have very nearly the same minimum energy. This implies that the ring and the collapsed structure are equally energetically favorable. It is only the hydrogen bonding involved in stacking that makes the ring a more preferable shape. A comparison of Figure 2 and Figure 8 shows that the ring is much more capable of hydrogen bonding than the collapsed structure. This indicates that the role of hydrogen bonding is essential to the formation and stability of nanotubes.

ACKNOWLEDGMENTS

The author thanks James Lewis for his valuable guidance; Dimitry Rekesh for his assistance in obtaining molecular structures; Otto F. Sankey, Alex A. Demkov and Thomas Drouillard for their assistance and insight; and Dionyssios Mintzopoulos, Matt Grumbach and Wolfgang Windl for the useful discussions. This work was performed under the auspices of the Arizona State University Physics Research Experience for Undergraduates Program, supported by the National Science Foundation and Arizona State University.

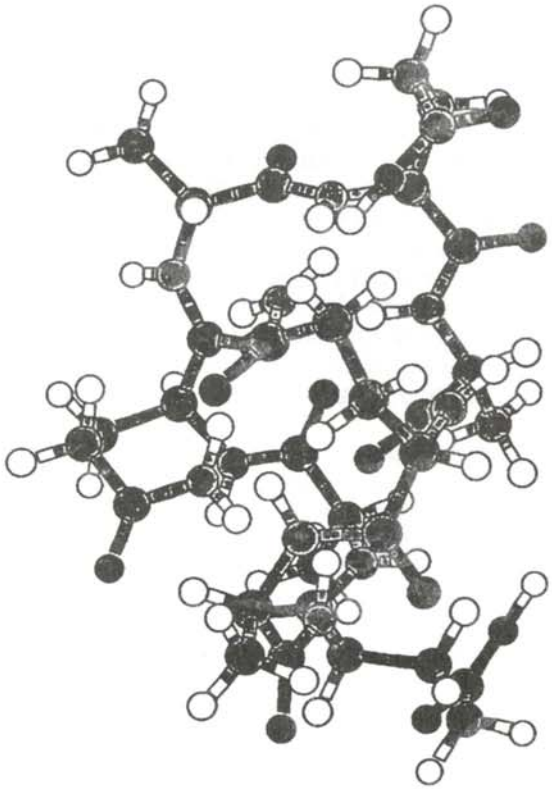

Figure 8
Collapsed cyclic octapeptide. This result is obtained when classical potentials are used, without constraints, to relax the structure. The image was produced using Xmol.

REFERENCES

* Present address of the author: Department of Physics, Colorado School of Mines, Golden, CO 80401. npawley@mines.colorado.edu
1. M.R. Ghadiri, J.R. Granja, R.A. Milligan, D.E. McRee, and N. Khazanovich, Nature, 366, (1993), p. 324.
2. M.R. Ghadiri, J.R. Granja and L.K. Buehler, Nature, 369, (1994), p. 301.
3. P.D. Santis, S. Morosetti and R. Rizzo, Macromolecules, 7, (1974), p. 52
4. F. Heitz, F. Kaddari, A. Heitz, H. Raniriseheno and R. Lazaro, Int. J. Peptide Protein Res., 34, (1989), p. 387.
5. L. Tomasic and G.P. Lorenzi, Helv. Chim. Acta., 70, (1987), p. 1012.
6. E. Ozeki, S. Kimura and Y. Imanishi, Int. J. Peptide Protein Res., 33, (1989), p. 14.
7. K.K. Bhandary and K.D. Kopple, Acta Cryst., C47, (1991), p. 1483.
8. D.S. Jois, K.R.K. Easwaran, M. Dednarek and E. Blout, Biopolymers, 32, (1992), p. 933.
9. K.C. Chou, A. Heckel, G. Némethy, S. Rumsey, L. Carlacci, and H.A. Scherage, Proteins, 8, (1990), p. 14.
10. M.J.E. Sternberg and J.M. Thornton, Nature, 271, (1978), p. 15.
11. J.R. Granja and M.R. Ghadiri, J. Am. Chem. Soc., 116, (1994), p. 10785.
12. N. Khazanovich, J.R. Granja, D.E. McRee, R.A. Milligan and M.R. Ghadiri, J. Am. Chem. Soc.., 116, (1994), p. 6011.
13. P. Hohenberg and W. Kohn, Phys. Rev. B136, (1964), p. 864.
14. W. Kohn and L.J. Sham, Phys. Rev, A140, (1965), p. 1133.
15. O.F. Sankey and D.J. Niklewski, Phys. Rev., B40, (1989), p. 3979.
16. P. Ordejón, D.A. Drabold, M.P. Grumbach and R.M. Martin, Phys. Rev., B48, (1993), p. 14646.
17. D.A. Drabold and O.F. Sankey, Phys. Rev. Lett., 70, (1993), p. 3631.
18. X.P. Li, R.W. Nunes and D. Vanderbilt, Phys. Rev, B47, (1993), p. 891.
19. E.B. Stechel, A.R. Williams and P.J. Feibelman, Phys. Rev, B49, (1994), p. 88.
20. F. Mauri and G. Gali, Phys. Rev. B50, (1994), p. 4316.
21. P. Ordejón, D.A. Drabold, R.M. Martin and M.P. Grumbach, Phys. Rev. , B51, (1995), p. 1456.
22. J. Ortéga, J.P. Lewis and O.F. Sankey, Phys. Rev., B50, (1994), p. 10516.

23. J.P. Lewis and O.F. Sankey, Biophys. J., 69, (1995), to be published.
24. H. Hellmanhn, *Einfuhrung in die Quantumchemie*, (Franz Deutsche, Leipzig, 1937).
25. R.P. Feynman, Phys. Rev. 56, (1939), p. 340.
26. M.R. Ghadiri, K. Kobayashi, J.R. Granja, R.K. Chadha and D.E. McRee, Communications, 34, (1995), p. 93.
27. S. Weiner, P. Kollman, D. Case, U. Singh, C. Chio, G. Algona, S. Profeta and P. Weiner, J. Am. Chem. Soc., 106, (1984), p. 765.

FACULTY SPONSOR

Dr. Otto F. Sankey
Department of Physics and Astronomy
Arizona State University
Tempe, AZ 85287-1504
Otto.Sankey@asu.edu

ELECTRODYNAMICS OF A CYLINDRICAL NEURON

Venkat K. Bhashyam *
Discipline of Physics
Northeast Missouri State University
Kirksville, MO 63501
received June 1, 1995

ABSTRACT

The electrodynamics of the transmission of a signal inside an infinitely long cylindrical neuron is shown with mathematical and physical rigor. Expressions for the potential difference between the two media, inside and outside a neuron, and the propagation current are obtained. The impedance for transmission of signal along a neuron is defined and derived.

INTRODUCTION

In a human body, the nervous system is the sensing, thinking and controlling system. The nervous tissue is made of nerve cells (or neurons) and supporting cells. The supporting cells hold the neurons in place. Nerve cells are attached to a long fibrous axon which transmits the nerve signals. The membrane of an axon contains more K^+ compared to its concentration outside. This causes the ions to leak out of the fiber, leaving a net negative potential inside due to the protein molecules. This potential is called the membrane potential and has a size of ≈ 70 mV. There is also a higher concentration of Na^+ outside, which can leak into the nerve fiber if the fiber is appropriately stimulated. This causes an action potential to appear at the point of the stimulation, which in turn sends an electric current along the inside of the axon. We will explore the electrodynamics of an idealized system of this kind and find an expression for the propagation current.

In neurophysical experiments, the most common observation is the potential difference between the interior and the exterior media of a neuron. These voltage measurements, in isolation, are not sufficient to explain the propagation of a signal along the length of the neuron. To have a better understanding of the signal, we need to know about the relationship between the current and voltage at various points along the neuron. Unfortunately, neurons are not as simply made as resistors and the propagation of a signal along them has a very different nature from the propagation of a signal along a resistor. The complexity arises when branching and the action potential are considered. [1]

Most studies of neurons begin with the cable equation, whose relationship to the underlying Maxwell's equations are not always clear. [2] In this paper, we study the electrodynamics of ion transport in neurons starting with Maxwell's equations as applied to an idealized cylindrically symmetric neuron of infinite length. We make use of this model and exploit the symmetry of Maxwell's equations to determine the voltage-current characteristics of a neuron.

SIGNAL TRANSMISSION IN A NEURON

Magnetic field of a neuron

A section of the model of the neuron we will discuss is shown in Figure 1. A cylindrical membrane separates the inside region of conductivity σ_1 and permittivity ε_1 from the outside region which has conductivity σ_2 and permit-

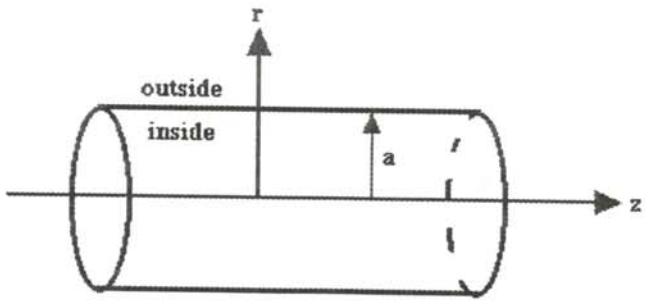

Figure 1
A section of an infinitely long cylindrical neuron. The z-axis is the direction of propagation of the signal.

Venkat is now a graduate student at Northwestern University, working towards a Ph.D. in physics. This research was done during his senior year at Northeast Missouri State University.

tivity ε_2.

Maxwell's equations for a system with permittivity, ε, and conductivity, σ, are [3]:

$$\nabla \times \vec{E} = \mu_o \frac{\partial \vec{H}}{\partial t} \quad (1)$$

$$\nabla \times \vec{H} = \sigma \vec{E} + \varepsilon \frac{\partial \vec{E}}{\partial t} , \quad (2)$$

Equations 1 and 2 can be combined to give:

$$\nabla^2 \vec{H} = \sigma \mu_o \frac{\partial \vec{H}}{\partial t} + \mu_o \varepsilon \frac{\partial^2 \vec{H}}{\partial t^2} , \quad (3)$$

For transverse magnetic fields in this cylindrical system, $H_r = H_z = 0$, so the only magnetic field is pointing in the θ direction:

$$H = H_\theta \hat{\theta} . \quad (4)$$

For an infinitely long fiber, the number of modes of oscillations of the field would be infinite. Therefore, we can write H_θ as a Fourier transform of h_θ in z, θ and t:

$$H_\theta = \iiint [h_\theta(r,\beta,\nu,\omega)]\, e^{[i(\beta z + \nu\theta + \omega t)]}\, d\beta\, d\nu\, d\omega , \quad (5)$$

where β, and ν are wave-numbers associated with z and θ ; ω is the frequency of the mode.

Using Equation 5, the Laplacian in cylindrical coordinates of H_θ becomes:

$$\nabla^2 H_\theta = \iiint \left(\frac{\partial^2 h_\theta}{\partial r^2} + \frac{1}{r}\frac{\partial h_\theta}{\partial r} - h_\theta \left[\frac{\nu^2}{r^2} + \beta^2 \right] \right) \left(e^{[i(\beta z + \nu\theta + \omega t)]} \right) d\beta\, d\nu\, d\omega \quad (6)$$

Combining Equation 3 and Equation 6 yields:

$$\frac{\partial^2 h_\theta}{\partial r^2} + \frac{1}{r}\frac{\partial h_\theta}{\partial r} - h_\theta \left[\frac{\nu^2}{r^2} + k^2 \right] = 0 , \quad (7)$$

where $k^2 = i\mu_o\omega\sigma^* + \beta^2$ and $\sigma^* = \sigma + i\varepsilon\omega$. Replacing r with $\rho = kr$ and writing $h_\theta = h_\theta(\rho,\nu)$ we get:

$$\frac{\partial^2 h_\theta(\rho,\nu)}{\partial \rho^2} + \frac{1}{\rho}\frac{\partial h_\theta(\rho,\nu)}{\partial \rho} - \left[\frac{\nu^2}{\rho^2} + 1 \right] h_\theta(\rho,\nu) = 0 \quad (8)$$

which is the modified Bessel's equation of order n. The solution to Equation 8 is given by:

$$h_\theta(\rho,\nu) = C_{1\nu} I_\nu(\rho) + C_{2\nu} K_\nu(\rho) , \quad (9)$$

where $C_{1\nu}$ and $C_{2\nu}$ are constants and $I_\nu(\rho)$ and $K_\nu(\rho)$ are cylindrical Bessel functions [4].

The real current density, J, inside the neuron of radius, a, can be defined as:

$$\vec{J}(r,z,\theta,t) = \iiint \frac{I(\beta,\omega,\nu)}{\pi a^2} \hat{z} + \alpha_1 \hat{r} + \alpha_2 \hat{\theta}\, e^{[i(\beta z + \nu\theta + \omega t)]}\, d\beta\, d\nu\, d\omega \quad (10)$$

where α_1 and α_2 are arbitrary functions of β, ω, ν, and $I(\beta,\omega,\nu)$ is the inverse Fourier transform of the current density along the z direction.

Equation 2 can be approximated as:

$$\nabla \times \vec{H} = \vec{J} \quad (11)$$

since the displacement current is very small compared to the real current.

Taking the curl of H as given in Equation 5 and combining Equation 10 and 11, we have:

$$-i\beta h_\theta \hat{r} + \left[\frac{1}{r}\frac{\partial}{\partial r}(r h_\theta) \right] \hat{z} = \frac{I(\beta,\omega,\nu)}{\pi a^2} \hat{z} + \alpha_1 \hat{r} + \alpha_2 \hat{\theta} \quad (12)$$

Integrating Equation 12 across the cross-sectional are of the neuron gives:

$$\int_0^{2\pi} \int_0^a \left(-i\beta h_\theta \hat{r} + \left[\frac{1}{r}\frac{\partial}{\partial r}(r h_\theta) \right] \hat{z} \right) \cdot (r\, dr\, d\theta)\hat{z} = \int_0^{2\pi} \int_0^a \frac{I(\beta,\omega,\nu)}{\pi a^2} \hat{z} \cdot (r\, dr\, d\theta)\hat{z} \quad (13)$$

Evaluating the dot product and carrying out the integration shows that:

$$h_\theta(r = a,\beta,\nu,\omega) = \frac{I(\beta,\omega,\nu)}{2\pi a} . \quad (14)$$

which agrees with Ampere's law in the β, ω, ν space.

Magnetic Field outside the neuron

In this region where $a/k < \rho < \infty$, we expect that $h_\theta(\rho,\nu)$ to be well behaved as $\rho \to \infty$. For $\rho \to \infty$, the expansions for $I_\nu(\rho)$ and $K_\nu(\rho)$ can be written as: [5]

$$I_\nu(\rho) = \frac{e^\rho}{\sqrt{2\pi\rho}} \; ; \; K_\nu(\rho) = \sqrt{\frac{\pi}{2\rho}}\, e^{-\rho} . \quad (15)$$

For a finite magnetic field outside a neuron, we need to have $C_{1\nu} = 0$, Therefore:

$$h_\theta(\rho,\nu) = C_{2\nu} K_\nu(\rho) . \quad (16)$$

But from Equation 14 and 16:

$$h_\theta(k_2 a,\nu) = \frac{I(\beta,\nu,\omega)}{2\pi a} = C_{2\nu} K_\nu(k_2 a) , \quad (17)$$

or:

$$C_{2\nu} = \frac{I(\beta,\nu,\omega)}{2\pi a} \frac{1}{K_\nu(k_2 a)} . \quad (18)$$

Therefore, outside of an infinite cylindrical neuron, the magnetic field is:

$$h_\theta(\rho,\nu) = \frac{I(\beta,\nu,\omega)}{2\pi a} \frac{K_\nu(k_2 r)}{K_\nu(k_2 a)} . \quad (19)$$

Magnetic field inside the neuron

In this region where $0 \le \rho \le a/k$, we expect $h_\theta(\rho,\nu)$ to be well behaved as $\rho \to 0$. For $\rho \to 0$, the expansions for $I_\nu(\rho)$ and $K_\nu(\rho)$ can be written as: [5]

$$I_\nu(\rho) = \frac{\left(\frac{\rho}{2}\right)^\nu}{\Gamma(\nu+1)} \; ; \; K_\nu(\rho) = \frac{(\nu-1)!}{\left(\frac{\rho}{2}\right)^\nu} \; . \qquad (20)$$

For a finite magnetic field outside a neuron, we need to have $C_{2\nu} = 0$, Therefore:

$$h_\theta(\rho,\nu) = C_{1\nu} I_\nu(\rho) \; . \qquad (21)$$

From Equation 14 and Equation 21:

$$h_\theta(k_1 a,\nu) = \frac{I(\beta,\nu,\omega)}{2\pi a} = C_{1\nu} I_\nu(k_1 a) \; , \qquad (22)$$

or:

$$C_{1\nu} = \frac{I(\beta,\nu,\omega)}{2\pi a} \frac{1}{I_\nu(k_1 a)} \; . \qquad (23)$$

Therefore, the magnetic field inside an infinite cylindrical neuron is:

$$h_\theta(\rho,\nu) = \frac{I(\beta,\nu,\omega)}{2\pi a} \frac{I_\nu(k_1 r)}{I_\nu(k_1 a)} \; . \qquad (24)$$

Electric Field inside the neuron

Using Equation 2, the electric field in the z direction inside the neuron can be expressed as:

$$E_{1z} = \iiint [\mathcal{E}_{1z}(r,\beta,\nu,\omega)]\, e^{[i(\beta z + \nu\theta + \omega t)]}\, d\beta\, d\nu\, d\omega \; , \qquad (25)$$

and Equation 5 for $H_\theta(r,z,\theta,t)$, we find that:

$$\mathcal{E}_{1z}(r,\beta,\nu,\omega) = \frac{1}{\sigma_1^* r} \frac{\partial [r h_\theta(r,\beta,\nu,\omega)]}{\partial r} \qquad (26)$$

Using Equation 23 for the magnetic field inside the neuron gives:

$$\mathcal{E}_{1z}(r,\beta,\nu,\omega) = \frac{1}{\sigma_1^* r}\left[h_\theta(r,\beta,\nu,\omega) + k_1 r C_{1\nu} \frac{\partial I_\nu(\rho)}{\partial \rho} \right] . \qquad (27)$$

Using the identity for the Bessel function $I_\nu(\rho)$,

$$\rho \frac{d}{d\rho} I_\nu(\rho) + \nu I_\nu(\rho) = \rho I_{\nu-1}(\rho) \; . \qquad (28)$$

we obtain:

$$\mathcal{E}_{1z}(a) = Z_1 I(\beta,\nu,\omega) \; , \qquad (29)$$

where $I(\beta,\nu,\omega)$ is the current in the neuron and Z_1 , the impedance of the inside of a infinite cylindrical neuron, given by:

$$Z_1 = \frac{1}{\sigma_1^* r}\left[\frac{1}{2\pi a}(1-\nu) + \frac{(k_1 a) I_{\nu-1}(k_1 a)}{2\pi a\, I_\nu(k_1 a)} \right] . \qquad (30)$$

Electric Field outside the neuron

Using equation 2, we get for the electric field outside the neuron, E_{2z}:

$$E_{2z} = \iiint [\mathcal{E}_{2z}(r,\beta,\nu,\omega)]\, e^{[i(\beta z + \nu\theta + \omega t)]}\, d\beta\, d\nu\, d\omega \; , \qquad (31)$$

Using Equation 5 for the magnetic field H_θ, we get

$$\mathcal{E}_{2z}(r,\beta,\nu,\omega) = \frac{1}{\sigma_2^* r} \frac{\partial [r h_\theta(r,\beta,\nu,\omega)]}{\partial r} \qquad (32)$$

Making use of Equation 23 for the magnetic field inside the neuron:

$$\mathcal{E}_{2z}(r,\beta,\nu,\omega) = \frac{1}{\sigma_2^* r}\left[h_\theta(r,\beta,\nu,\omega) + k_2 r C_{2\nu} \frac{\partial K_\nu(\rho)}{\partial \rho} \right] . \qquad (33)$$

Using the identity for the Bessel function $K_\nu(\rho)$:

$$\rho \frac{d}{d\rho} K_\nu(\rho) + \nu K_\nu(\rho) = -\rho K_{\nu-1}(\rho) \; . \qquad (34)$$

we find that the electric field outside the neuron is:

$$\mathcal{E}_{2z}(a) = Z_2 I(\beta,\nu,\omega) \; , \qquad (35)$$

where $I(\beta,\nu,\omega)$ is the current and Z_2, the impedance outside of an infinitely long cylindrical neuron, is given by:

$$Z_2 = \frac{1}{\sigma_2^* r}\left[\frac{1}{2\pi a}(1-\nu) + \frac{(k_2 a) K_{\nu-1}(k_2 a)}{2\pi a\, K_\nu(k_2 a)} \right] . \qquad (36)$$

Voltage-Current relationship

To find a relationship between the potential inside a neuron at various points compared to outside of the neuron, we consider the boundary, as shown in Figure 2. Along the loop A -> B -> C -> D:

$$V(z+dz) + E_{1z}(a,z,t)dz - V(z) + E_{2z}(a,z,t)dz = 0 \; . \qquad (37)$$

Using the traditional definition of a derivative, this can be written as:

$$\frac{\partial V}{\partial z} = -[E_{1z}(a,z,t) + E_{2z}(a,z,t)] \; . \qquad (38)$$

We now can write an expression for the longitudinal current flowing inside the fiber and the voltage across the membrane. Combining Equations 29, 35 and 38:

$$\frac{\partial V}{\partial z} = -\iiint [I(\beta,\nu,\omega)]\, e^{[i(\beta z + \nu\theta + \omega t)]}\, (Z_1 + Z_2) d\beta d\nu d\omega \; . \qquad (39)$$

Equation 39 is valid for any arbitrary function for Z_1 and Z_2. To find a relationship between current and voltage in real variables, we need to consider the case when Z_1 and Z_2 are constants, independent of β, ν and ω. We would be

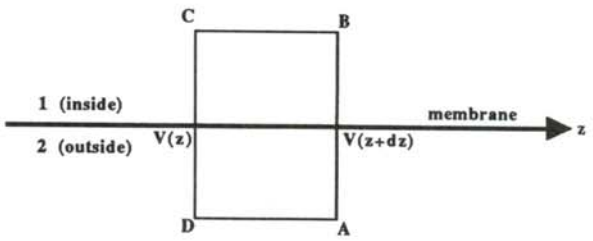

Figure 2

The membrane separating the two media. The inside of the neuron (1) is at a higher potential than the outside of the medium (2). V(z) is the potential difference between the two media at a particular z.

able to make this assumption when the second terms in Equations 30 and 36 do not vary appreciably compared to the first terms. In this case:

$$\frac{\partial V}{\partial z} = -(Z_1 + Z_2)\, i(z,\theta,t) \ . \qquad (40)$$

where $(Z_1 + Z_2)$ represents the impedance in the signal transmission and $i(z,\theta,t)$ represents the amount of current propagating at a particular position and time. Equation 40 can be found in neurophysical text books, [2] but the assumptions in the derivation of Equation 40 are not clear in the texts. Here we have rigorously shown the derivation and its underlying relationship with Maxwell's equations.

ACKNOWLEDGMENT

The author would like to thank his advisor Professor Mohammad Samiullah for suggesting this problem and patiently checking his calculations.

REFERENCES

* Present address of author: Department of Physics, Northwestern University, Evanston, IL 60208. V-Bhashyam@NWU.edu

1. W.F. Ganong, Review of Medical Physiology, 10th ed., Lange Medical Publications, (1981).
2. A.C. Scott, Neurophysics, John Wiley & Sons, Inc., (1977).
3. D.J. Griffiths, Introduction to Electrodynamics, 2nd ed., Prentice Hall, Inc., (1989).
4. G.N. Watson, A Treatise on the Theory of Bessel Functions, 2nd ed., Cambridge University Press, (1944).
5. I.S. Gradshteyn and I.M. Ryizhik, Table of Integrals, Series and Products, Academic Press, (1980).

FACULTY SPONSOR

Dr. Mohammad Samiullah
Division of Science
Science Hall 262
Northeast Missouri State University
Kirksville, MO 63501

EXPERIMENTAL VERIFICATION OF ELECTRON NANODIFFRACTION THEORY WITH CARBON NANOTUBES

Scott D. Packard*
Arizona State University
Tempe, AZ 85287-1504
received August 23, 1995

ABSTRACT

Carbon nanotubes serve as samples of known structures for which the diffraction intensities can be calculated and compared with those obtained by a Scanning Transmission Electron Microscope. An asymmetry is expected in the diffraction pattern from these nanotubes from the bending of the electron beam by the projected potential of the carbon layers. The intensity distributions of the electron nano-diffraction patterns observed experimentally show agreement with theory. This agreement between predicted and observed patterns allows for extended application of nanodiffraction to the determination of small, complex object geometries such as the end morphologies of carbon nanotubes.

INTRODUCTION

Recent technological advances in electron microscopy have improved the control of the electron beam. The technology now exists to create electron diffraction patterns from extremely small areas of a specimen, sizes on the order of nanometers. Although the literature shows qualitative agreement between experimental results and theoretical predictions [1], there does not yet exist quantitative proof of the electron nanodiffraction theory. This experiments was designed to test the diffraction theory in a situation where a significant asymmetry in the diffraction pattern is expected.

Carbon nanotubes are concentric sheets of graphitic carbon wrapped into a cylindrical shape. A typical nanotube could have a dozen such carbon sheets, resulting in a tube diameter of about 10 nm and a length of up to a micron. The tubes are created by an intense DC discharge between carbon electrodes in an inert gas. They have been referred to as buckytubes because each cylindrical layer of graphitic carbon can be thought of as a buckyball extended by a tube of hexagonal graphitic carbon.

Scott is a senior physics major at Cornell University. This research took place during the summer after his junior year during an NSF sponsored program at Arizona State University. Scott plans to attend graduate school in either medical physics or nuclear engineering. He will most likely study functional brain imaging with magnetic resonance. In his spare time, he enjoys watching, playing and coaching ice hockey.

When viewed from a direction perpendicular to the axis, the carbon nanotubes have a curvature that increases towards the ends of the tubes. Because of this changing curvature, the carbon sheets are expected to act as small prisms, bending the electron beam and biasing the diffraction pattern toward one side. [2]

The carbon nano-tubes used in this experiment have many interesting characteristics worthy of study. Their potential use as nano-wires has drawn much attention recently. There are many other possible microelectronics applications that depend on the physical characteristics of the nano-tubes. [3]

It is hypothesized that nanotubes could form a fiber unequalled in strength per weight. It is also possible that such a structure might have a tendency to regenerate itself under certain conditions if damaged. The possible uses for an enhanced carbon fiber are endless. [9]

THEORY

A field emission gun (FEG) provides an extremely bright source that can generate a powerful electron beam that can be reasonably approximated as completely coherent. [2] This coherent source of electrons allows for the analysis of very small areas of the specimen. Diffraction patterns can be detected from areas on the order of 1 nm in diameter. This level of precision allows for the capture of structural data from a very small area and consequently allows a more detailed evaluation of the overall structure of the specimen.

The incoming electrons are diffracted by the potential, as

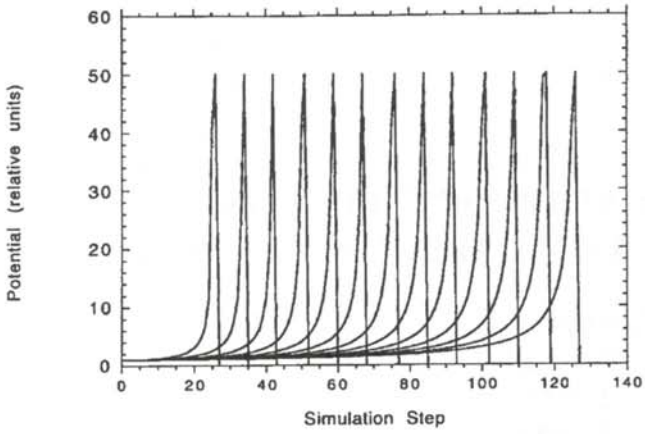

Figure 1
Potential for individual carbon shells as a function of the distance from the center of the tube (simulation steps)

seen by the beam, created by the carbon layers of the carbon nanotube. In a carbon nanotube, each layer of carbon is wrapped into a cylindrical sheet. If the finite size of the carbon atoms is neglected, the potential of a single cylinder can be approximated by an inverse cosine curve. The potential function for each layer, as shown in Figure 1, can be summed over the numbers of layers in the tube to give the potential for a carbon nanotube. For a symmetrical tube (with 15 layers, separated by 0.34 nm; outer diameter 15 x 0.34 nm and inner diameter 3 x 0.34 nm), the potential function is as shown in Figure 2. The singularities that occur in the inverse cosine function at $\pi/2$ have been removed by arbitrarily selecting a maximum projected potential value of 50 units (which scales to 2600 Volt Å). This value is large enough to represent a maximum while eliminating many mathematical difficulties.

The potential in Volts can be calculated from the Fourier coefficients $V(h)$ by:

$$V(h) = \frac{47.87801\ \Phi(h)}{\Omega}\ , \qquad (1)$$

where h is the reciprocal lattice vector, Ω is the volume of a unit cell [4], and $\Phi(h)$ is defined as:

$$\Phi(h) = \sum f_i(h)\ e^{2\pi i\, h\, r_i} \qquad (2)$$

where $f_i(h)$ are properties of the atoms which make up the sheets.

If the beam is traveling in the z direction, the 2-dimensional potential, $\phi(x,y)$ seen by the beam can be calculated from the 3-dimensional potential, $\phi(x,y,z)$ by integrating over the z variable. According to the phase-object approximation, we can neglect the lateral spread of the electron beam as a result of Fresnel diffraction or scattering, so the wave function of the electrons after they pass through the sample is given by:

$$\psi(x,y) = e^{-i\sigma\phi(x,y)}\ , \qquad (3)$$

where σ is an interaction constant. [5]

The wave function is divided into real and imaginary components, which are summed over the number of carbon shells in the nanotube. It is important to account for the fact that the incoming electron beam is very small, but not zero. A beam of width 5.5 Å , 13 simulation steps, can be simulated by a Gaussian function of the form:

$$G(x) = \exp\left[\frac{-(x-\lambda)^2}{(13)^2}\right] \qquad (4)$$

where λ is the center of the electron beam and x describes the position in the beam. The theoretical intensity pattern in real space is found by multiplying the complex wave-function, $\psi(x,y)$ by the Gaussian distribution representing the finite width of the beam.

This real space data can be converted into Fourier space data by:

$$F = \int \psi(x,y)\, e^{2\pi i(ux+vy)}\, dx\, dy\ , \qquad (5)$$

The resulting intensity pattern in reciprocal space is directly comparable to an electron diffraction pattern.

For carbon atoms perpendicular to the electron beam, $f_i(h) = 2.509$ Volt Å. The unit cell of graphitic carbon has a volume of 17.746 Å^3 and two carbon atoms per unit cell. The interaction constant $\sigma = 9.24\text{x}10\text{-}4$. [4] Inserting these values into Equation 2 gives:

$$\Phi(0) = 2\, f_i(0) = 5.018\,. \qquad (6)$$

From Equation 1, the potential (in Volts) at the center of the tube is:

$$V(0) = 47.87801 \times \frac{5.018}{17.746} = 13.533 \qquad (7)$$

When the incident beam is perpendicular to the $n = 11$ carbon layers, the integral over $\phi(x,y,z)$ is:

$$\phi(x,y) = 13.533\ \text{V x } n \text{ x } 3.4\ \text{Å} = 506.15\ \text{VÅ} \qquad (8)$$

However, a correction must be made for the fact that the electron beam travels through two half shells, each with a potential. This correction requires that $\phi(x,y)$ be doubled.

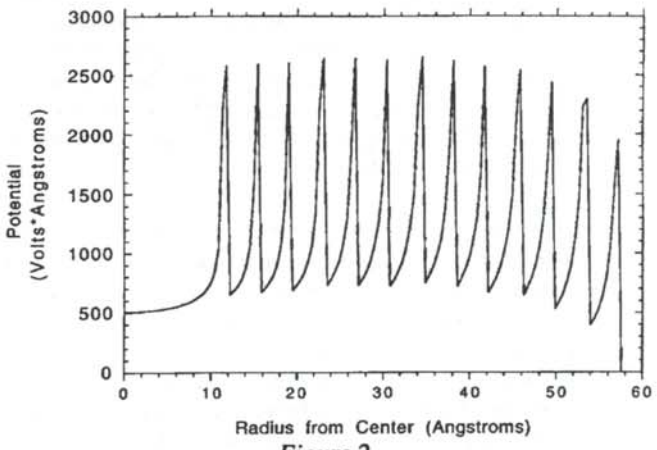

Figure 2
Sum of the individual shells (shown in Figure 1) across the tube.

Inserting this corrected value into Equation 3 gives:

$$\psi(x,y) = e^{-i\,0.9152} \qquad (9)$$

With this wave function, the curve in Figure 2 can be scaled to represent the projected potential perpendicular to the axis of the nanotube. It is important to correct for the finite width of the carbon atoms. The values in Figure 3 are smoothed by averaging each value with its adjacent values. This correction corresponds to a smoothing of the projected potential of 1.2 Å, approximately the size of the carbon atoms in the cylindrical sheets.

The electron beam is described by Figure 3, scaled by the wave function given in Equation 9 and the Gaussian function of Equation 4. These real-space predictions are transformed into reciprocal space by a computer program utilizing a Fast Fourier Transform algorithm. [8] The program outputs the real and imaginary components of the transformed function. The plot of the magnitude of these results is equivalent to:

$$I = \left| F\cos(\sigma\phi) + F\sin(\sigma\phi) \right|^2 \qquad (10)$$

which is the intensity of the diffracted beam. This intensity is directly comparable to the line intensity profiles taken from the experimentally measured diffraction patterns.

EXPERIMENTAL METHOD

The carbon nanotube specimen used in this study was created by a variant of the Kratschmer-Huffman arc-discharge technique. [6] An intense DC voltage of 26-28 V with 70 A was applied across the carbon electrodes. When the residue was examined with an electron microscope, carbon nanotubes were found, varying in thickness from approximately 3 to 30 sheets, with lengths up to 1 μm. There were a wide variety of tube shapes, including typical cylindrical tubes as well as those with bends, changing thickness and changing helicity.

A HB-5 scanning transmission electron microscope

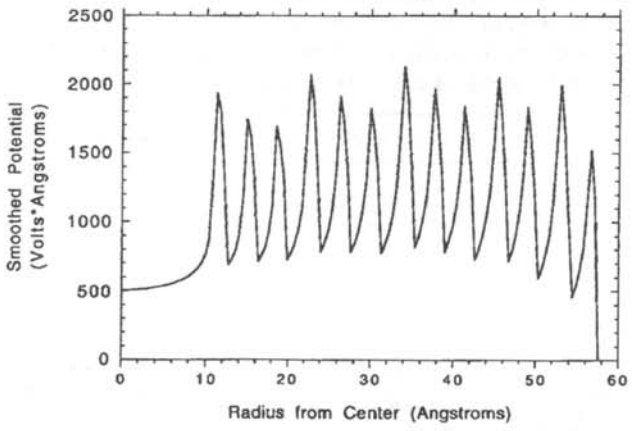

Figure 3
Projected potential of the nanotube after smoothing with the averaging function.

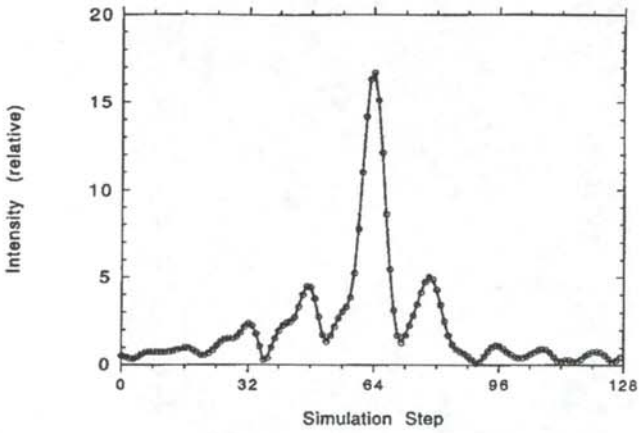

Figure 4
Theoretical Fourier calculation of the smoothed projected potential.

(STEM) was used to generate and collect the diffraction patterns.[7] The HB-5 operated at 100 kV and performed nanodiffraction, a form of convergent beam electron diffraction. [2] A charge coupled device (CCD) digitally captured the diffraction patterns produced with the sample. The CCD camera allows superior intensity and distance measurements. The line intensity profile of the diffraction patterns was extracted by computer analysis of the data. Many digital line profiles across diffraction patterns were compared to the theoretical line intensities generated from the Fourier transform of Equation 5. The diffraction patterns were examined using bright-field and dark-field STEM imaging [2] and were recorded with a VCR system and 35 mm film as well as the CCD camera.

RESULTS

Figure 4 shows the theoretically calculated line intensity, while Figure 5 shows a sample line intensity profile extracted from a diffraction pattern from Tube C. It is

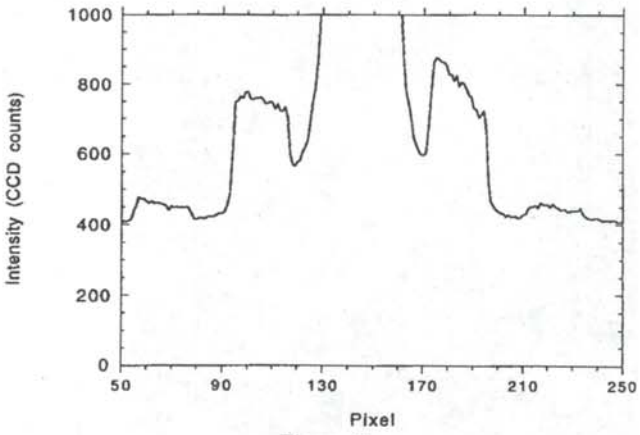

Figure 5
Left side of Tube C, a symmetrical cylindrical tube, demonstrates the asymmetry in the intensity of its diffraction pattern.

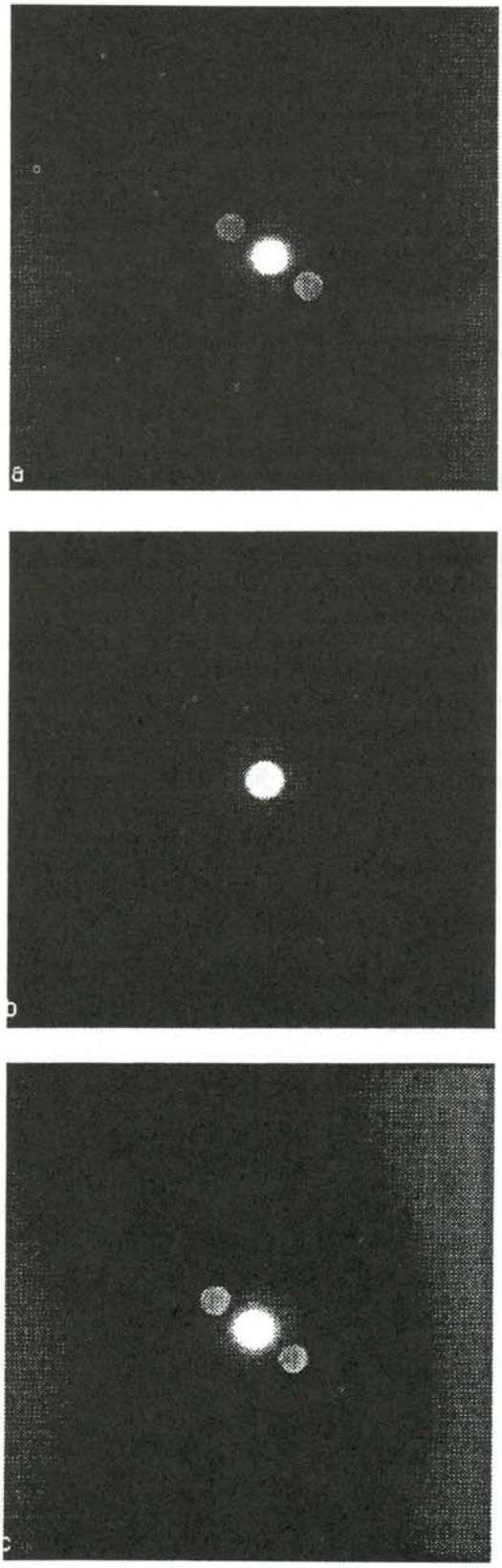

Figure 6
Diffraction patterns from Tube C. a) left side, b) center, d) right side of the tube.

evident that the predicted asymmetry does exist in this nanotube. Tube C is a typical, symmetric, strongly diffracting circular nanotube. It serves as an especially good example because of the high intensity of its diffraction pattern.

Figure 6 shows the diffraction pattern as seen on the low light level TV monitor of the HB-5. Figure 6a shows the diffraction pattern produced by the left side of the tube, Figure 6b by the center of the tube and Figure 6c by the right side of the tube. The electron beam was first placed on the left side of the tube as it appeared in the bright-field imaging device. Note that one of the first order diffraction peaks is significantly greater than the other. In this case, the higher peak is on the opposite side from the beam because of the post specimen lens crossover and an arbitrary rotation of the bright-field image. More importantly, with the same STEM instrument configuration and with the electron beam placed on the right of the nanotube, the stronger first-order peak switched from the right side to the left side (see Figure 7). This result was the same for all of the diffraction patterns taken of tubes without highly distorted morphologies.

It has been found that not all nanotubes have a circular cylindrical shape. [10] A few appear to have a polygonal (probably pentagonal) cross section, so that there are flat sides on the tubes which make the tubes appear asymmetrical in projection. Tube E (shown in Figure 8) is such an asymmetrical sample. Its diffraction pattern showed a similar, but stronger peak asymmetry. One side of the central maximum diffracts more strongly than the other. When the beam is placed on the opposite side of the tube (Figure 9), the larger first-order peak switches sides.

The ratio of the intensity on both sides of the central maximum are found by integration of the area under the line intensity curves for all the experimental data and for the theoretical calculations. The experimental ratio can be tuned by simulating the background with a Gaussian spread from the central maximum. Subtracting this integral from the integral of the experimental data yields a more precise ratio of the peak intensities. A listing of some of these ratios is given in Table 1.

These ratios show that for all but the most distorted nanotubes, placement of the beam on the opposite side of the tube inverts the relative first-order peak intensities. This ratio varied from 1.021 to 1.661. For the theoretical tubes, this ratio was 1.954 for a near-edge centered beam with a non-smoothed potential. This ratio reduced to 1.208 when the finite width of the carbons atoms was taken into

Nanotube	Left Side Ratio	Right side Ratio
b	1.341	1/1.176
c	1.157	1/1.250
d	1.143	1/1.098
g	1.661	1/1.400
h	1.056	1/1.020
Theory	1.954	1/1.954
Smoothed Theory	1.208	1/1.208

Table 1
Intensity ratios for non-distorted and asymmetric tubes.

account. For a simulated beam placed half way from the center of the tube to its edge, the ratio of intensities was 1.653, which reduced to 1.044 when the smoothing function was applied. The ratio of the intensities should be greater near the edge of the tube as there is more curvature in the tube at this region. The ranges of the intensity ratios of the experimentally determined data match well with the theoretically predicted values.

This agreement is not as strong with the asymmetric tubes as with the symmetric ones. This difference is probably due to the strange morphologies within the highly asymmetric tubes. These differences are not taken into account in the simulation and large structural differences cause significant changes in the line intensity of the diffraction patterns. Small asymmetries appear to result in small perturbations of the diffraction intensities and do not greatly disturb the ratio of the first-order peaks.

ACKNOWLEDGMENTS

The author thanks John M. Cowley for his guidance, Michael R. Scheinfein and Paul R. Perkes for their assistance, and the Materials and Electrochemical Research Corporation, Tuscon, AZ, for supplying the specimen used in this project. This work was performed under the auspices of the Arizona State University Physics Research Experience for Undergraduates Program, supported by the National Science Foundation and Arizona State University.

REFERENCES

* Present address of author: Department of Physics, Cornell University, 109 Clark Hall, Ithaca, NY 14853. packard@ruph.cornell.edu

1. M.J. Hÿtch, J.P. Chevalier, Ultramicroscopy, 58, (1995), p. 114.
2. J.M. Cowley, Electron Diffraction Techniques, J.M. Cowley, ed., Volume 1, Oxford Science Publications, Oxford, (1992).

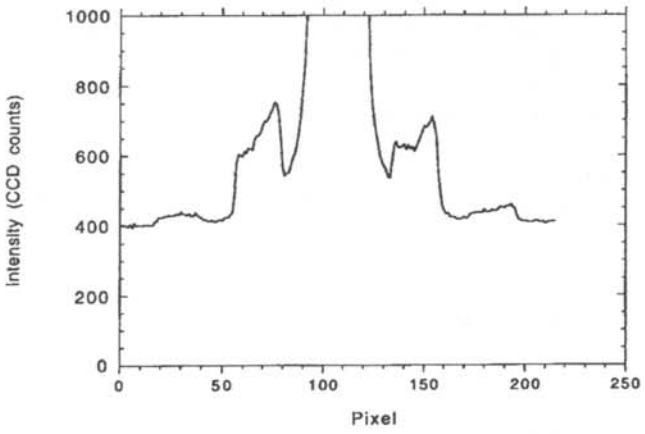

Figure 7
Right side of Tube C, a symmetric cylindrical tube, demonstrates the asymmetry in the intensity of its diffraction pattern.

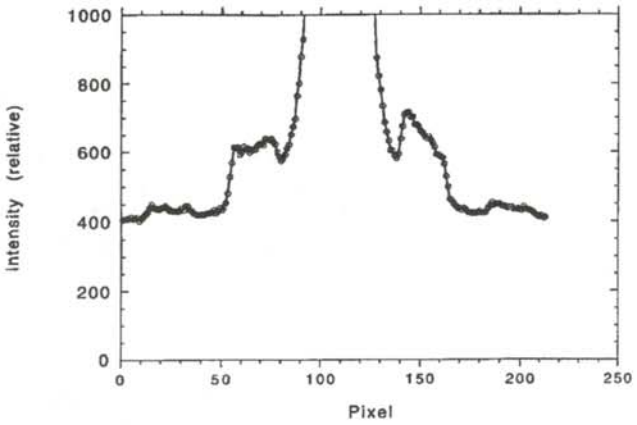

Figure 8
Tube E, although asymmetric, also demonstrates the asymmetry in its diffraction pattern predicted by nano-diffraction theory.

3. P.M. Ajayan and S. Iijima, Nature, 361, (1992), p. 333.
4. International Tables for Crystallography, Volume C, A.J.C. Wilson, Ed., (1992), pp. 223-225.
5. J.M. Cowley, Diffraction Physics, North Holland, Amsterdam, (1981), Chapters 11,13.
6. T.W. Ebbesen and P.M. Ajayan, Nature, 358, (1992), p. 220.
7. J.M. Cowley, Ultramicroscopy, 49, (1993), p. 4.
8. The Fourier transform program was supplied by Dr. M. Scheinfein.
9. P.E. Ross, Scientific American, (Dec 1991), p. 24.
10. M. Liu, J.M. Cowley, Ultramicroscopy, 53, (1994), pp. 333-342.

FACULTY SPONSOR

Dr. John M. Cowley
Department of Physics and Astronomy
Arizona State University
Tempe, AZ 85287-1504
Cowleyj@phyast.la.asu.edu

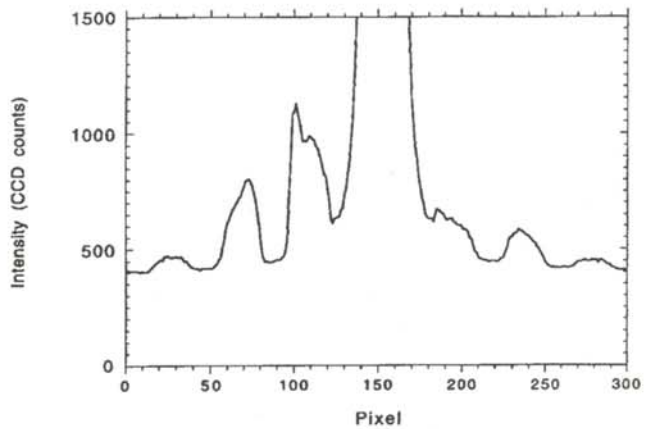

Figure 9
The opposite side of Tube E from Figure 8

AN ALTERNATIVE TO DARK MATTER: DO GALACTIC ROTATIONAL VELOCITY CURVES SUGGEST A MODIFICATION OF NEWTON'S LAW OF GRAVITATION?

Eric Barnes *
Discipline of Physics
Northeast Missouri State University
Kirksville, MO 63501
received April 24, 1995

ABSTRACT

The rotational velocity curve for galaxy NGC 3198 was analyzed. A fit to the observational data was found. This function was combined with a general mass function for a galaxy to obtain a distance-dependent Newton's constant. This new function replaces the constant G_N in Newton's law of gravitation, and forms the basis for a non-Newtonian explanation for the dark matter problem.

INTRODUCTION

In 1932, Jan van Oort discovered that the Milky Way galaxy only has one third of the mass needed to describe the observational distribution of mass in the form of stars. [1] Many, if not most, astrophysicists and astronomers now believe that stars make up less than about 10 percent of the mass of the universe. The rest of the universe is unseen, dark matter which only interacts with ordinary matter through gravity. This belief is based on the fact that calculations differ from observation. However, there are alternative explanations where one attempts to understand the disagreement between the calculations and the observations by modification of either Newton's second law of motion or Newton's law of gravitation, both of which enter the calculation. Einstein's theory of gravity can be seen as a suggestion of such a modification. In the past Newtonian approximation of Einstein's theory, a distance dependent gravitational constant emerges if one insists on writing the gravitational potential in the form: [2]

$$\phi(r) = \frac{G(r)\,M}{r}. \qquad (1)$$

Eric graduated from Northeast Missouri State University in May of 1995. This research encompasses work done during both his junior and senior years. He is preparing to enter Louisiana State University as a graduate student in physics and astronomy. Eric divides his time between working, questioning the laws of nature, golfing and attempting to please his robust, supportive and genetically gifted parents.

The most compelling evidence of the disagreement between the calculations and observations comes from the rotational velocity curves of many galaxies. These curves describe the rotational velocity of a galaxy as a function of the distance away from the center of the galaxy. According to Newtonian mechanics, the radial velocity, $v(r)$, is given as:

$$v(r) = \sqrt{\frac{G_N\,M(r)}{r}}\,, \qquad (2)$$

where G_N is Newton's constant, r is the radial distance and $M(r)$ is the amount of mass in the galaxy up to the distance r. From this expression, it is seen that once all the mass of the galaxy is included, $v(r)$ should drop off as $1/r^{1/2}$, as seen in the motion of the planets in the solar system. But, the observation of stars in many galaxies, an example of which is shown in Figure 1, has shown that the velocity remains constant up to very large distances. [3] It can be seen from Equation 2 that if $M(r) \approx r$, then $v(r)$ will be constant. Since $M(r)$ must go like r to explain the rotational velocity curve of Figure 1 and since there is not much luminous mass at the edge of the galaxy, one postulates that there is 'dark matter'. The distribution of the 'dark matter' should be such that there is more near the edge of the galaxy than at the center, hence the proposal of dark matter halos around galaxies. [4]

The nature of 'dark matter' has been debated over the last decade. Many particles and objects have been proposed as 'dark matter' candidates, including exotic objects such as WIMPS (weakly interacting massive particles), brown dwarfs and massive neutrinos. As of now, there is no direct evidence for the existence of any of these dark matter candidates. [5]

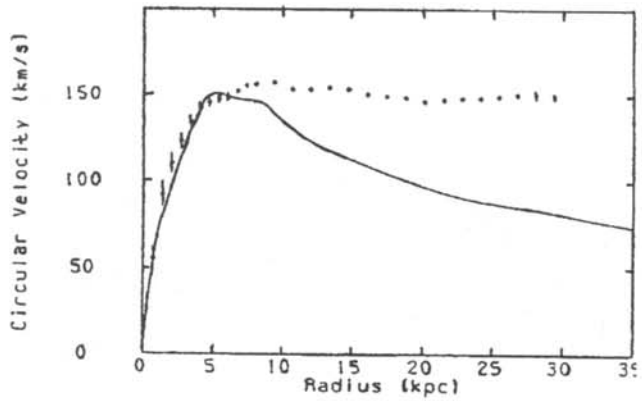

Figure 1

The observational rotational velocity data points (dots) and the calculated rotational velocity curve based upon Newtonian gravity and dynamics (line). This figure is taken from reference 3.

Are there other ways to explain the discrepancy between the observations and the calculations? The derivation of Equation 2 gives some clues. The derivation assumes the validity of Newton's law of gravitation and Newton's second law of motion, both of which may take on different forms at a large distance scale, such as a galactic scale. One proposal is a modification of the second law of motion. [6] This theory is based on the idea that Newton's second law does not hold in the limit of small acceleration. A simple modification of the second law is made to test this idea. [6] The second law formula:

$$\vec{F}_{net} = m\,\vec{a} \tag{3}$$

is replaced by:

$$\vec{F}_{net} = m\,\mu\!\left(\frac{a}{a_o}\right)\vec{a}\ , \tag{4}$$

where a_o is a universal acceleration constant and $\mu(a/a_o)$ is a function which equals 1 if $a \gg a_o$ and equals a/a_o if $a \ll a_o$. This new dynamics was able to generate velocity curves which have the same qualitative features as the observations [6,7] What we propose is a modification of Newton's law of gravitation which also leads to velocity curves similar to those experimentally observed for a galaxy.

THE MODEL

We explore the possibility that Newton's gravitational constant is not constant, but dependent on distance between two objects. Newton's law of gravitation would be modified as:

$$F = G(r)\frac{M\,m}{r^2}\hat{r}\ , \tag{5}$$

where the function $G(r)$ replaces Newton's constant G_N. The function $G(r)$ must be such that it yields Newton's constant in the limit of distances much less than the galactic scale and also in the limit of distances much greater than the galactic scale. The galactic scale plays a special role because the anomaly present in the velocity curves is shown only at this scale. This is similar in spirit to the universal acceleration parameter, a_o mentioned earlier. Furthermore, a special role for the galactic scale may explain why galaxies are of comparable sizes. The question we ask is: what is the form of the function $G(r)$ which will explain the anomalous rotational velocity curve shown in Figure 1 and also be consistent with experiments in the laboratory?

The velocity curve of Figure 1 is used to find the appropriate function $G(r)$ using:

$$G(r) = \frac{r\left[v^2(r)\right]}{M(r)}\ . \tag{6}$$

We start out by fitting the observed $v(r)$ to a function and then use models for galaxies to get $M(r)$. The two are combined in Equation 6 to give the desired function $G(r)$. The general features of all the observed velocity curves are similar. We chose, for the sake of concreteness, to study the rotational velocity curve for galaxy NGC 3198 which is shown in Figure 1. The fitting function, $v(r)$ must reproduce the asymptotic behavior of the rotational curves and include a small 'hump" just before the flatness begins.

Constructing G(r)

We express the velocity function, found from curve fitting, in terms of a dimensionless variable:

$$\bar{r} = \frac{r}{\xi}\ , \tag{7}$$

where ξ is a galactic length scale. The velocity function has the form:

$$\frac{v(\bar{r})}{v_o} = \frac{\bar{r}\,e^{-\bar{r}} + \tanh(\bar{r})}{\sqrt{1+\frac{\bar{r}}{n}}}\ , \tag{8}$$

where v_o and n are needed to fit the curve. The first part of the numerator gives the small hump, the hyperbolic tangent function gives the semi-asymptotic behavior and the denominator "kills" the velocity when the distance is much greater than the galactic scale.

The mass density for a galaxy was assumed to be:

$$\rho(r,\theta,\phi) = \begin{cases} B_s\,e^{-\bar{r}} & \text{spherical distribution} \\ B_s\,e^{-\bar{r}}\delta(\theta-\frac{\pi}{2}) & \text{cylindrical distribution} \end{cases} \tag{9}$$

Where B_s and B_c are the mass densities at the centers of the spherical and cylindrical distributions respectively. [7] We define dimensionless mass functions for the two types of galaxies: $M_s(r)/M_G$ and $M_c(r)/M_G$ where M_G is the total mass of the galaxy:

$$\begin{aligned} M_G &= 8\pi\,B_s\,\xi^3 \quad \text{spherical galaxy} \\ M_G &= 4\pi\,B_c\,\xi^3 \quad \text{cylindrical galaxy.} \end{aligned} \tag{10}$$

These dimensionless mass functions can be found by integrating $\rho(r,\theta,\phi)$ from 0 to r to get the mass enclosed up to a distance r in the galaxy:

$$\frac{M_{s,c}(r)}{M_G} = \left[1-\frac{1}{2}\gamma(3,\frac{r}{\xi})\right]\ , \tag{11}$$

where $\gamma(3,r/\xi)$ is the gamma function. This mass enclosed function has two limiting values:

$$\lim_{\frac{r}{\xi}\to 0} \frac{M_{s,c}(r)}{M_G} = \frac{\left(\frac{r}{\xi}\right)^3}{6}$$

$$\lim_{\frac{r}{\xi}\to \infty} \frac{M_{s,c}(r)}{M_G} = 1 \qquad (12)$$

Substituting Equations 8 and 11 in Equation 6, one obtains the desired expression for $G(r)$:

$$G(r) = \frac{v_o^2\, r\left[\frac{r}{\xi} e^{-\frac{r}{\xi}} + \tanh\left(\frac{r}{\xi}\right)\right]^2}{\xi\left(1+\frac{r}{\xi}n\right)\left(1-\frac{1}{2}\gamma(3,\frac{r}{\xi})\right)} \quad . \qquad (13)$$

When $r \ll \xi$, we expect that $G(r)$ should equal the usual Newton's constant, G_N. Taking this limit of Equation 13, we find that:

$$\lim_{\frac{r}{\xi}\to 0} G(r) = \frac{24\,\xi\, v_o^2}{M_G} \quad . \qquad (14)$$

The right side of Equation 14 is set equal to G_N. Thus, we obtain an explanation of the origin of G_N in terms of galactic parameters.

For the purposes of plotting our data, we define $g(\bar{r})$ which measures $G(\bar{r})$ as a fraction of G_N:

$$g(\bar{r}) \equiv \frac{G(\bar{r})}{G_N} \quad . \qquad (15)$$

The limiting behavior of $g(r)$ is given by:

$$\lim_{\bar{r}\to 0} g(\bar{r}) \to 1 \quad \text{(by construction)}$$

$$\lim_{\bar{r}\to \infty} g(\bar{r}) \to \frac{n}{24} \quad . \qquad (16)$$

The value of n could be found by satisfying the necessary dynamical requirement for intergalactic gravitational force. [8]

Figure 2 shows plots of $g(\bar{r})$, $v(\bar{r})/v_o$ and $M(\bar{r})/M_o$

DISCUSSION AND INTERPRETATION

The problem with which this research deals arose from the discrepancy between calculations and the observed galactic rotation velocity curves. We used published observational data to form the basis of the study of distance dependent modification of Newton's law of gravitation. [2] Fitting the data to an expression for $v(r)$, we developed a function, $G(r)$, which replaces Newton's constant in the law of gravitation.

To get a physical picture of the r-dependent Newton's constant, we look at Figure 2. The gravitational constant function first drops and then begins to rise slowly to a constant value at infinity. This behavior is clearer if one examines the gravitational force. The gravitational potential energy, U, is given by:

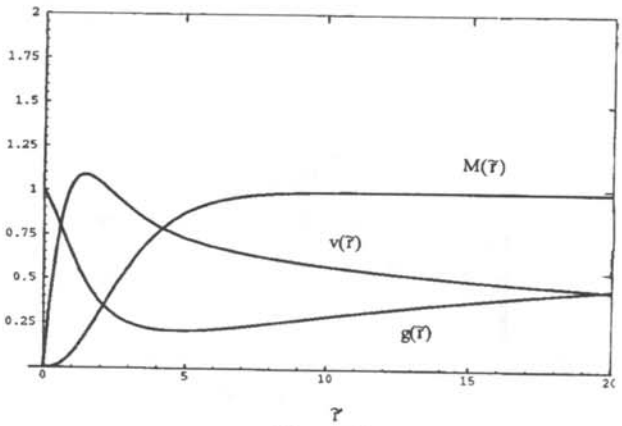

Figure 2

The functions $g(\bar{r})$, $v(\bar{r})/v_o$ *and* $M(\bar{r})/M_o$ *versus* $\bar{r}$ *for* n *equal to 24.*

$$U = -\frac{\mathcal{G}(r)\, M\, m}{r} \quad , \qquad (17)$$

where $\mathcal{G}(r)$ is related to $G(r)$ in the force equation. The force can be found from Equation 18:

$$\vec{F} = -\vec{\nabla}U = \frac{\frac{\partial}{\partial r}\mathcal{G}(r)\, M\, m}{r}\hat{r} - \frac{\mathcal{G}(r)\, M\, m}{r^2}\hat{r} \quad . \qquad (18)$$

If $\mathcal{G}(r)$ has a negative slope, the two terms add. This occurs when r is small and the second Newtonian term dominates. This addition of terms gives a larger force than classically calculated. This larger force corresponds to a higher rotational velocity. When the derivative of $\mathcal{G}(r)$ with respect to r is zero, the force and the rotational velocity should be the same as calculated from Newton's law of gravitation. As r increases, the first term will dominate the behavior of force. The first term is completely non-Newtonian.

ACKNOWLEDGMENTS

The author would like to thank his faculty research supervisor, Dr. Mohammad Samiullah, for the inspiration and guidance he provided.

REFERENCES

* present address of author: 303 N. Stanton Street, Lebanon, IL 62254.

1. J.H. Oort, Bull. Astr. Inst. Netherlands, 6, (1932), p. 249.
2. S. Weinberg, Gravitation and Cosmology, John Wiley & Sons, Inc., New York, (1972), p. 228.
3. R. Sancisi and T.S. Van Albada, IAU Symposium 117, Dark Matter in the Universe, D. Reidel, (1958), p. 71.
4. S.M. Farber and J.S. Gallagher, Annual Review of Astronomy and Astrophysics, 17, (1979), p. 135.

5. M.S. Turner, FERMILAB conf-92/382-A, January 1993.
6. M. Milgrom, the Astrophysical Journal, 270, (1983), pp. 365-370.
7. M. Milgrom, The Astrophysical Journal, 270, (1983), pp. 371-383.
8. F. Zwicky, Helv. Phys. Acta, 6, (1933), p. 110.

FACULTY SPONSOR

Dr. Mohammad Samiullah
Discipline of Physics
Division of Science
Science Hall 262
PO Box 828
Northeast Missouri State University
Kirksville, MO 63501-0828

PREPARING A MANUSCRIPT FOR PUBLICATION

Rexford E. Adelberger, Editor

Perhaps the most important thing for you to keep in mind when you write a manuscript which you intend to submit for publication to the Journal of Undergraduate Research in Physics is that the audience that will be reading the paper are junior or senior physics majors. They are knowledgeable about physics, but unlike you, they have not spent as much time trying to understand the specific work which is being reported in your paper. They also can read English well and expect the paper to be written by a colleague, not a robot or an 'all-knowing' computer. There is a big difference between the comments you write in the margin of your lab notebook or what you might write in a technical brief and what you should present in a paper for publication in a scientific journal.

There is a significant difference between a Journal article and keeping a journal. Your laboratory data book should be the journal of what you did. It contains all the data, what you did (even if it was an attempt that turned out to be wrong), as well as comments as to what you were thinking at that time. The Journal article is an discussion of how you would do the research without excursions along blind alleys and hours spent collecting data that were not consistent. The reader should not necessarily be able to completely reproduce the work from the Journal article, but the reader should be able to understand the physics and techniques of what was done.

How a person uses Journal articles to find out about new ideas in physics is often done in the following way. A computerized search using key words in abstracts is done to see what work has been done in the area of interest. If the abstract seems to be about the question, the body of the paper is tracked down and read. If the reader then wants to find out the finer details of how to reproduce the experiment or the derivation of some equation, the author is contacted for a personal in-depth conversation about the more subtle details.

The general style of writing that should be followed when preparing a manuscript for publication in the Journal is different from what you would submit to your English literature professor as a critique of some other work. The narrative of the paper is intended to do three things: 1) to present the background necessary for the reader to appreciate and understand the physics being reported in the paper; 2) discuss the details of what you did and the implications of your work; 3) lead the reader through the work in such a way that they must come to the same concluding points that you did. When finished with your paper, the reader should not have to go back and try to decide for themselves what you did. Your narrative should lead them through your work in an unambiguous manner, telling them what to see and understand in what you did. The interpretation of the data or calculations should be done by the writer, not the reader. The interpretation of your results is the most important part of the paper.

You should take care to make sure that the material is presented in a concise logical way. You should make sure that your sentences do not have too many dependent clauses. Overly complicated sentences make the logic of an argument difficult to follow. You should choose a paragraph structure that focuses the attention of the reader on the development of the ideas.

A format which often achieves these aims is suggested below:

ABSTRACT : An abstract is a self contained paragraph that concisely explains what you did and presents any interesting results you found. The abstract is often published separately from the body of the paper, so you cannot assume that the reader of the abstract also has a copy of the rest of the paper. You cannot refer to figures or data that is presented in the body of the paper. Abstracts are used in computerized literature searches, so all key words that describe the paper should be included in it.

INTRODUCTION: This is the section that sets the background for the important part of the paper. It is not just an abbreviated review of what you are going to discuss in detail later. This section of the narrative should present the necessary theoretical and experimental background such that a knowledgeable colleague, who might not be expert in the field, will be able to understand the data presentation and discussion. If you are going to use a particular theoretical model to extract some formation from your data, this model should be discussed in the introduction.

Where appropriate, factual information should be referenced using end-notes. When presenting background information, you can guide the reader to a detailed description of a particular item with the statement such as: *"A more detailed discussion of laminar flow can be found elsewhere 1"*. If you know where there is a good discussion of some item, you don't have to repeat it, just guide the reader to the piece.

How one proceeds from this point depends upon whether the paper is about a theoretical study or is a report on an experiment. I will first suggest a format for papers about experimental investigations and then one that describes a theoretical derivation.

Experimental Investigations

THE EXPERIMENT: This section guides the reader through the techniques and apparatus used to generate the data. Schematic diagrams of equipment and circuits are often easier to understand than prose descriptions. A statement such as *"A diagram of the circuit used to measure the stopping potential is shown in Figure 6"* is better than a long elegant set of words. It is not necessary to describe in words what is shown in a diagram unless you feel that there is a very special part which should be pointed out to the reader. If special experimental techniques were developed as part of this work, they should be discussed here. You should separate the discussion of the equipment used to measure something from your results. This section should not include data presentations or discussions of error analysis.

DATA PRESENTATION AND INTERPRETATION OF RESULTS: This is the most important section of the paper. The data (a plural noun) are the truths of your work. This section should lead the reader through the data and how errors were measured or assigned. The numerical data values are presented in tables and figures, each with its own caption, e.g.. *"The results of the conductivity measurements are shown in Table 3"*. It is difficult to follow narratives where the numerical results are included as part of the narrative. Raw, unanalyzed data should not be presented in the paper. All figures and tables should be referred to by their number. Any figure or table that is not discussed in the narrative should be eliminated. Items which are not discussed have no place in a paper.

A Theoretical Study

THE MODEL: This part should consist of a theoretical development of the constructs used to model the physical system

under investigation. Formulae should be on separate lines and numbered consecutively. The letters or symbols used in the equations should be identified in the narrative, e.g.. *The potential can be approximated as:*

$$W \approx Z - \sigma(\rho) \ , \qquad (1)$$

where Z is the number of protons and σ is the screening constant that is dependent on the charge density, ρ, of the inner electrons of the K and L shells. If you wish to use this formula at a later time in the narrative, you refer to it by its number, e.g.. *"The straight line fit shown in Figure 3 means that we can use Equation 1 to extract a value of..."*

CALCULATIONS: This section presents a summary and discussion of the numerical results calculated from the model. The results should be presented in tables or graphs, each with a caption. A table or graph which is not discussed in the narrative should be eliminated. Data that are not interpreted by the writer have no place in a paper. One should reference numerical results that are used in the calculations and come from previous work done by others .

The following sections pertain to both types of papers.

CONCLUSIONS: It is indeed rare that one can come to clear and meaningful conclusions in one paper. I do not know of many papers where this section should be included.

REFERENCES: All references, numbered in order from beginning to end of the paper, are collected together at the end of the paper. You should be aware of the following format:

If the reference is a text-

1. A.J. Smith and Q.C.S. Smythe, Electromagnetic Theory, Addison Wesley, New York, (1962), p. 168.

If the reference is a journal-

2. J. Boswain, Journal of Results, 92, (1968), pp. 122-127.

If the reference is unpublished-

3) R.J. Ralson, private communication.

ACKNOWLEDGMENTS: This short section should acknowledge the help received (that is not referenced in the previous section) from others. This is where you would give credit to a lab partner or someone in the machine shop who helped you build a piece of equipment.

OTHER ADVICE

TABLES AND FIGURES are placed by the layout editors at the corners of the page to make the format attractive and easy to read. Often a figure is not on the same page as the discussion of the figure. Each table or figure should be numbered and have a caption which explains the figure. Readers scan papers by looking at the figures and data tables before they read the narrative of the work. Take care to put enough information in the caption of a figure or table so that the reader can get some feeling for the meaning of the data presentation. All lines shown on graphs should be identified, e.g.. *"The dashed line is drawn to guide the eye"* or *"The solid line is a fit to the data using the Ising model"*

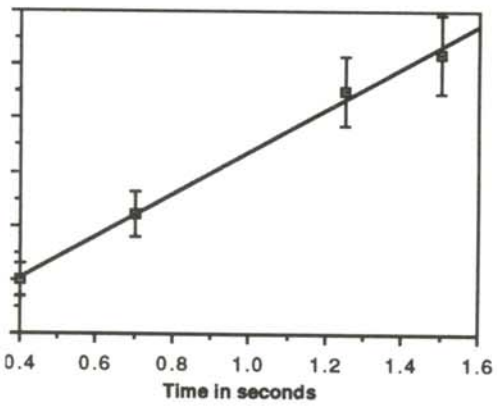

Figure 1

A graph of the measured thrust of a D-2 model rocket engine as a function of time. The line drawn is the least squares fit straight line to the data.

State	*Experimental eV*	*Theoretical eV*
3S	*5.15±.01*	*5.13*
4S	*1.89±.02*	*1.93*
3P	*2.96±.02*	*3.02*

Table 1

Energy states found in the numerical search. The accepted values for these states are also listed.

An example of a graph of a set of data is shown in Figure 1. The graph is sized by the range of data points. The bottom left point does not have to be the point (0,0). Error bars are shown with the data points. A graph with all the data points clustered in one small corner and lots of white space does not help the reader get a feeling of the dependence of your data. Be careful that the figures you present are not too busy; too much information on a figure makes it difficult to pick out the important parts.

NUMBERS AND UNITS Any experimentally measured data presented in tables (such as shown in Table 1), should include an uncertainty. You should use scientific notation when presenting numbers, $(7.34 \pm .03) \times 10^7$ eV. Take care that you have the correct number of significant digits in your results; just because the computer prints out 6 digits does not mean that they are significant. You should use the MKS system of units.

STYLE It is often helpful to make a flow chart of your paper before you write it. In this way, you can be sure that the logical development of your presentation does not resemble two octopuses fighting, but that it is linear.

One generally writes the report in the past tense. You already did the experiment. You also should use the third person neuter case. Even though you might have done the work by yourself, you use "we". e.g.. *"We calculated the transition probability for..."* It is often confusing when you begin sentences with conjunctions. Make sure that each sentence is a clear positive statement rather than an apology.

There are a few words or phrases you should be careful about using. ***Fact*** - this is a legal word. I am not sure what it means in physics. ***Proof or prove*** - These words are meaningful in mathematics, but you can't prove something in physics, especially experimental physics. ***The purpose of this experiment is...*** Often it is necessary to do the experiment to complete the requirements for your degree. You do not need to discuss the purposes of the experiment. ***One can easily show that...*** - Don't try to intimidate the reader. What if the reader finds it difficult to show? Remember that the reader of your paper is a senior in college! ***It is obvious that... or One clearly can see....*** - Such statements only intimidate the reader that does not find your work trivial. What is obvious to someone who has spent a lot of time thinking about it may not be obvious to the reader of your paper.

The Journal of Undergraduate Research in Physics

The Journal of Undergraduate Research in Physics is the journal of Sigma Pi Sigma and the Society of Physics Students. It is published by the Physics Department of Guilford College, Greensboro NC 27410. Inquiries about the journal should be sent to the editorial office.

The Journal of Undergraduate Research in Physics ISSN 0731-3764

Editorial Office -

The Journal of Undergraduate Research in Physics
Physics Department
Guilford College
Greensboro, NC 27410
910-316-2279 (voice)
910-316-2951 (FAX)

Editor -

Dr. Rexford E. Adelberger
Professor of Physics
Physics Department
Guilford College
Greensboro, NC 27410
ADELBERGERRE@RASCAL.GUILFORD.EDU

The Society of Physics Students

National Office -

Dr. Dwight Neuenschwander, Director
Ms. Sonja Lopez, SPS Supervisor
Society of Physics Students
American Institute of Physics
1 Physics Ellipse
College Park, MD 20740
301-209-3007

President of the Society -

Dr. Fred Domann
Department of Physics
University of Wisconsin at Platteville

President of Sigma Pi Sigma -

Dr. Jean Krisch
Department of Physics
University of Michigan, Ann Arbor

- EDITORIAL BOARD -

Dr. Raymond Askew
Space Power Institute
Auburn University

Dr. László Baksay
Department of Physics & Astronomy
The University of Alabama

Dr. Dwight Neuenschwander
Department of Physics
Southern Nazarene Univesity

Dr. A. F. Barghouty
Department of Physics
Roanoke College